School of Engineering, Cardiff University

Fadi Atallah

Student Number: C1834762

20/21 – EN3100 Project

Dissertation Report

23 April 2021

Declaration

I hereby declare that, except where I have made clear and full reference to the work of others, this submission, and all the material (e.g. text, pictures, diagrams) contained in it, is my own work, has not previously been submitted for assessment, and I have not knowingly allowed it to be copied by another student. In the case of group projects, the contribution of group members has been appropriately quantified. I understand that deceiving, or attempting to deceive, examiners by passing off the work of another as my own is plagiarism. I also understand that plagiarizing another's work, or knowingly allowing another student to plagiarize from my work, is against University Regulations and that doing so will result in loss of marks and disciplinary proceedings. I understand and agree that the University's plagiarism software 'Turnitin' may be used to check the originality of the submitted coursework.

Signed: Fadi Atallah

Total number of words = 10,030 Total number of pages = 60

Evaluation of the Porosity and Surface Roughness of Additive Manufactured Aluminium Parts

Name: Fadi Atallah

Supervisor: Dr Debajyoti Bhaduri

Abstract

The surface quality of additive manufacturing products has attracted the commitment of numerous mechanical researchers due to its continuous quality improvement and prevention of surface-initiated cracking making it useful in the automotive and aerospace industries. This study experiments the nature of extracting optimal top surface roughness parameters and in-depth porosity analysis to interpret the characteristics of the Selective Laser Melting process.

A 3-factor, 3-level full factorial Design of Experiments with a total of 27 tests of experimental data has been gathered, use of Two and Three-way ANOVA testing has been conducted on the derived and fundamental variables respectively, main effect and 3D plots have also tested the relationships and significance of the factors on one another. The following quantities have been segregated, correlated, and non-parameter tests have been conducted to optimise the process parameters and achieve the best surface and porosity quality within an AlSi10Mg Aluminium alloy.

AlSi10Mg cubes were fabricated using the laser powder bed fusion (LPBF) process. Independent parameters gain insight into the effect of energy density and scan speed on porosity and surface roughness. Results showed the impact of laser energy density on SLM AlSi10Mg manufactured parts being experimented and concluded that medium energy density values of = 156.25 Jmm^{-1} reduces porosity to a minimum, whereas the top roughness optimises at around 133.3 Jmm^{-1}. Moreover, considerable differences in roughness appeared using different parameters and optimised surface quality was obtained at 6.81 µm that would still be high and inapplicable in the tested applications.

Acknowledgement

The author would like to express his great gratitude and thanks for all the generous advice and encouragement provided by Dr Debajyoti Bhaduri in this dissertation. It has been a great honour to work under his supervision.

The author would also like to extend his deep thanks and sincere appreciation to Mr Ben Mason and Miss Tina Dehban's aid in mechanical polishing. Many thanks to Professor Peter Morgan and Mr Carlos de la Torre for their statistical assistance. Dr Frank Lekkon and Mr Andrew Randore for preparing and manufacturing the samples. Last but not least, Dr Emmanuel Brousseau for his lab induction and overall support.

Contents

List of Figures

List of Tables

Chapter 1

Introduction

"When you can measure what you are speaking about, and express it in numbers, you know something about it, but when you cannot express it in numbers, your knowledge is of a meagre and unsatisfactory kind; it may be the beginning of knowledge, but you have scarcely, in your thoughts advanced to the stage of science." (Lord Kelvin, 1883).

1.1 Project Background

Additive manufacturing (AM) presents exciting new opportunities for manufacturers, especially designs that have previously been impossible to achieve using traditional manufacturing processes. This relates to the concept of designing for performance rather than design for manufacture where complex parts can be easily made providing a clear advantage over subtractive manufacturing methods. The simplicity in which designs are sketched, modelled and exported as STL files led to a growth in the field. This simplified method has been more favourably followed than the Volumetric approach which takes into consideration layer distribution, tool paths, and stress balancing that is far more complex than what can be imagined.

Selective Laser Melting (SLM), also known as Powder bed fusion (PBF), is a rapid prototyping additive manufacturing technique designed to operate under high laser power-density towards melting and fusing metallic powders (Aboulkhair et al. 2014). Cost reduction is making SLM more popular, but since it is an additive manufacturing method as-built layer upon layer, it develops high roughness values on top and side surfaces that raises a concern in industrial application. (Hirata et al. 2020).

1.2 Aims and Objectives

Previous studies have not focused enough on the SLM output properties of AlSi10Mg aluminium alloy. Therefore, this project fulfils to evaluate the effects of different manufacturing parameters on the following Alumunium cubes.

The research objectives are to:

- Test the applicability of material usage in the automotive and aerospace industries.
- Establish and highlight statistical correlations in AM parameters.
- Assess the surface roughness and porosity of AlSi10Mg fabricated parts and understand the mechanisms of pore formation as an approach towards eliminating them.

1.3 Research Motivation

Material and Application

This study deals with AlSi10Mg aluminium alloy, which is of excellent use for its improved dynamic and hardenability properties due to its 4% magnesium percentage. It has been verified that for the following comparison of SLM against conventional cast aluminium with the same chemical composition, the hardness property has shown to be 60% higher in the SLM manufacturing sample than the cast one (Boschetto et al. 2017). Among Aluminium-based alloys, this specific alloy is highly demanded in railways, aeronautics, and aerospace because of its low density causing a reduction in fuel cost, low thermal expansion (accounting for less shrinkage), good castability (producing fully dense parts), and excellent weldability properties enabling its application in the electronic packaging and automotive sector. (Kempen et al. 2011).

Most of the available researched resources investigated stainless steel alloys which hold high strength, and corrosion resistance for typical use in heat exchanges and exhaust manifolds (Aboulkhair et al. 2014). Some other examples like Titanium which compromises analysis with high strength to weight ratio are useful in applications similarly to AlSi10Mg that not many researchers considered experimenting with. Magnesium has a high susceptibility to evaporate producing parts with reduced Mg content compared to metal powder. Investigations could be carried to highlight the effect of the composition changes on the material's mechanical properties.

Figure 1.1: Pelton Wheel – (Energy Education, 2019).

SLM's outstanding ecological indicators save resources leaving zero wastes inspired by nature's Biomimicry. Another indicator is its eco-design optimisation that allows complex parts to be created monolithically, and hence lightweight structuring with a typically 50% weight reduction (Martin et al. 2017).

In addition to the previously mentioned applications, and Impulsive Pelton Wheel bucket example shown in Figure 1.1 is of excellent usage using this Aluminium alloy since the process allows the creation of thin walls accounting for the geometry's complex design and curvatures. However, to date, industries still require higher precision values, thus making the following manufactured parts not suitable yet (Larrosa et al. 2018). Making a need for post-processing procedures where its usage potential is available after mechanical or laser polishing, reducing the surface roughness value to less than 0.5 µm.

Chapter 2

Literature Review

2.1 Powder Structure and Flowablilty

2.1.1 Powder Manufacturing

Powder handling is the process of pouring powder into a reservoir of sufficient volume. In regards to recycling, usually, two-thirds of raw unused powder and a third of the overflow recycled feed powder take part in the AM processes. A similar fact applies to the percentage of glass powder being used in glass factories for the "Press and Blow" manufacturing method making it more profitably and sustainably desirable (MC Glass - 2020). Powder Handling and Recycling are both important factors to consider when manufacturing. Additionally, flow characteristics, particle's size, distribution, shape and micro-structure all contribute to the sample's output quality marking powder flowability of most overall importance.

A flow characteristic with high value can easily fill a mould cavity steadily and uniformly. Manufacturing in the powder metallurgy process involves sintering and several other operations such as machining and heat treatments where particles are heated below their melting point to bind (Kempen et al. 2011). Metallic powders possess different properties with sizes ranging between 20 – 60 µm; depending on the selected powder manufacturing process different sizes and shapes are to be expected.

Starting with the atomisation process, molten metal powders using this method are forced through an orifice with high pressure of either gas or liquid. The following method is mostly applicable for low melting point metals and perfect for aluminium alloys due to their corrosive action on orifices at high temperatures. Gas atomization is the main commercial process that provides fine powder structures, compared to water atomised ones which form irregular non-circular shaped molecules. For brittle materials, a crushing process is alternatively used by a powder fusion method. Large masses are first powdered, then injected into heavy crushing rolls and finally into milling machines to produce fine grades of powder.

2.1.2 Fusion Mechanism

In powder manufacturing, three main fusion mechanism choices are of availability:

1. Solid-state sintering
2. Liquid-phase sintering
3. Chemically induced binding

Briefly, Solid State Sintering (SSS) refers to the process of particle fusion without melting; in which the whole procedure completes in its solid-state, heated at around half the melting temperature. Liquid phase sintering and partial melting (LPS) are alternatively undergone where powder particles are bound to molten binders acting like glue triggering stickiness with temperature. Chemically induced sintering is another method used for ceramic materials or aluminium alloys bound in the presences of Nitrogen (N_2) forming Aluminum Nitride (AlN) Nanoparticles.

2.2 Factors Affecting Final Quality

Differences within a pack of binder's size and density in a process result in output problems. In structural material application, if the binder is smaller than the particle, better packing and less shrinkage would be of notice leaving fewer gaps within the sample. However, causing a disadvantage if the heat source is cut rapidly; as the molten binder particles have high viscosity and not adequate heating would leaving out pores between the particles requiring a further

Figure 2.1: Spoon of sugar and flour.

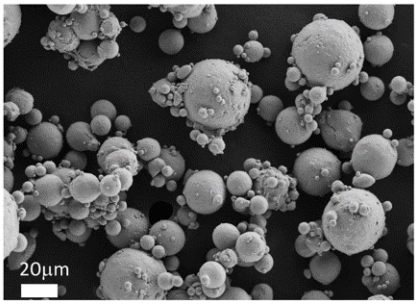

Figure 2.2: Gas atomized powder particles.

furnace post-processing procedure. Also, in case differences in densities between the binder and structural material is present, the following may lead to separations, and thus porous outcomes as well (Read et al. 2015).

The shape is regarded as the main factor in ensuring consistent layering. If the powder was not spread in a consistent and even manner, then porosity would arise compromising its mechanical properties. Spherical shaped powders shown in Figure 2.2, are the ones present in the high-end quality gas atomisation method preferred due to their good flowability characteristics. However, their cost accounts for the expense.

In considering the size, if a particle gets smaller, friction forces on it increase thus reducing flowability. i.e. similar to the analogy of tipping flour and sugar of a spoon shown in Figure 2.1. As the spoon is held at an angle, the larger particle (sugar) would fall and the flour would stay still until tipped at a greater angle. On the other hand, manufacturing from smaller particles provides a better accuracy and surface finish, allowing the creation of thinner layers, which are of more use in real-life applications as shown in the Pelton Wheel example (Figure 1.1). Smaller powder particles need sintering at lower temperatures when compared to larger ones (Hirata et al. 2020), where the diffusion rates increase exponentially with temperature and modelled using the Arrhenius Equation.

$$k = e^{\frac{-E_a}{RT}} \tag{2.1}$$

2.3 Porosity Optimisation

2.3.1 Time and Temperature

When loose powders at the build platform are maintained at elevated temperature, lower regions becomes denser than upper ones that evolved into uneven pores and can be resolved by controlling the cooling rates. Porosity levels could be reduced if subjected to longer sintering times or higher temperatures, but such solutions would cause Solid-State grains to expand and correspondingly output lower hardness values, providing potential for crack creations and fracture development. Also, the shorter the time needed for layer formation, the more economically viable the manufacturing process is of use in industry. However, rapid exposure time leaves unmolten particles in the solid-state, and thus gas between in between (Kempen et al. 2011). Thus, time and temperature should be optimised for obtaining the lowest porosity percentages.

Residual stress analysis shown in Figure 2.3 views the resultant tensile stresses developed within the structure. As layers were added, those stresses could lead to the formation of cracks and thus improve the structural strength.

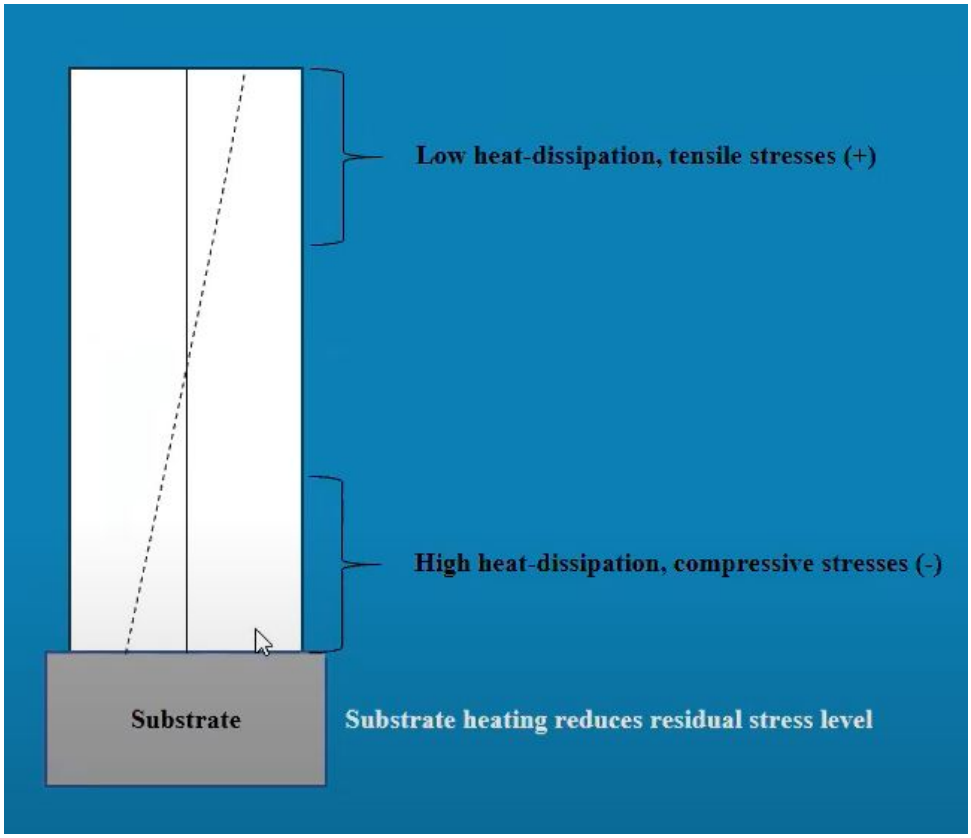

Figure 2.3: Heat Dissipation affect on stresses. – (Wong and Hernandez 2012)

2.3.2 Laser Power

The powering source for SLM systems is considered to be high; in Stereolithography (SLA): Power needed ranges up to 0.1 in the Photopolymerization process with scan speed $v \sim 1m/s$. For Fused Deposition Modelling (FDM): $\sim$ 10 W laser power is needed for melting the filament. Whereas SLM requires 100 – 1000 W for powder melting at much higher scanning speeds, making laser power a major process parameter in such systems.

$$\phi = \frac{\mathrm{P}}{v \times H_S \times t} \tag{2.2}$$

Very high laser power shown by the term P in equation 2.2 is proportional to ϕ or E as described in other books. If increased to a very high value, the powder would potentially create turbulence and form defects as it evaporates corresponding to an increase in the number and size of pores (Wong and Hernandez 2012).

Insufficient melting, thus low energy density value would leave spaces between powders. For this reason, there is a need for powder scan speed and power compatibility. i.e. 1200 mms^{-1} scan speed, 1500 or 1900 all could produce the same output density if it has been compromised for the right laser power, linking roughness and porosity measurements subject to the following quantities.

Optimising energy densities with laser power scanning speeds is of vital importance to identify high densification within a metal piece and avoid keyhole porosity development. Gas induced porosity forms due to the escape of gases in case of an incomplete melting. i.e. inputting less amount of energy would result in an incomplete melting. Therefore, high densification has a major contribution to the result. Figure 2.4 shows how a porous material appears under a microscope, marking the furthest one on the right (d) with the highest and (a) with the lowest porosity.

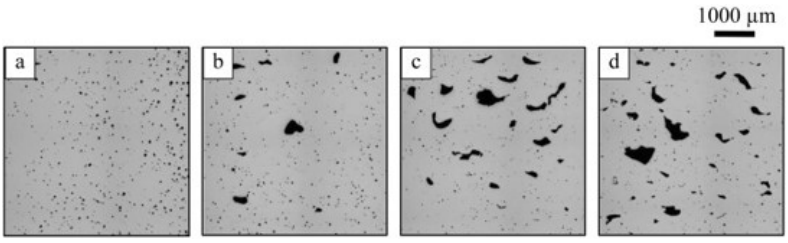

Figure 2.4: Varying porosity outcomes – (Read et al. 2015).

2.4 Arial Parameters (S_a, S_q, S_{sk}, S_{ku}, S_p, S_v, S_z)

2.4.1 Overview

Irregularities in material's surface characteristics cause roughness, which affects the impact on quality and performance. Although a high value is often undesirable, it is expensive to be controlled. For standardised statistical moments, the first moment provides a mean value, the second moment illustrates variance and spread, third Skewness and fourth Kurtois; showing heaviness distribution around the tail.

- S_a: represents the average roughness of the surface's departure ± mean plane.
- S_q: tests the root mean square value of the heights; equivalent to the standard deviation.
- S_{sk}: measures the degree of surface deviation asymmetry about the mean plane; useful in monitoring wear conditions.
- S_p: measures the height of the highest peak within a certain area on a surface.
- S_{ku}: indicates the presence of peaks or valleys on a surface.
- S_v: represents the absolute height values of the largest pit within a certain areal surface.
- S_z: represents a measure of the sum of the largest peak height value and the largest pit depth value within an area defined in Equation 2.3:

$$S_z = S_p + S_v \tag{2.3}$$

Topography is a term used to describe the entire geometric information associated with a surface shape and its features. Surface topography is mainly defined by three parameters (S_a, S_q, and S_z). Most methods link surface fatigue to roughness using S_a and S_q due to the suitability of these two parameters in gear-life predictive calculations, and their prevalence linked more to their historic availability on common profilometers than their accuracy in classifying gear surfaces. However, the parameter S_z is limited to its ability in differentiating surface quality; it accounts for the highest and largest pit on a surface showing the most extreme instances affected by outliers. Additionally, it is influenced by valley depth and of less detrimental importance to gear performance than peak height.

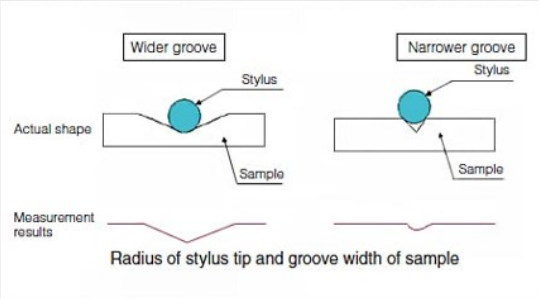

Figure 2.5: S_a against inputted parameters (P_D, E_T and H_S).

Figure 2.6: Talysurf PGI – (Taylor & Hobson, 2020).

2.4.2 Contact Stylus Profilometer

Under the branch of topography, surface texture extracts the feel after applying a series of filters on the measured face to extract roughness parameters. Values of such textures are heavily dependant on the computed data sets processed using the topographical data. Preceding different roughness measuring methods (contact or optical), different data sets are expected to generate, each relating to the measurement technology being adopted and the way it has interacted with the material's surface.

In a 2D conventional mechanical stylus with a profile, the tip dimensions are of fundamental importance; decreasing the tip size or radius applies more stress on the element causing scratches but detects finer details as shown in Figure 2.5. Therefore, an optimum combination between the spherical tip size and pressure applied needs to be obtained not to scratch the surface nor obtain inaccurate results.

An example of a mechanical stylus is "Talysurf PGI NOVUS" shown in Figure 2.6 used for surface finish and contour. The following instrument was designed with a class-leading 20 mm gauge range and 0.2 nm resolution capability to measure surface finish (roughness, form, waviness) in bearings, injectors and precision component. Providing instant measurement analysis feedback, where areal measurements can be also possibly experimented with from multiple closely spaced 2D scans of the targeted area.

2.5 Statistical Analysis Overview

Mean, mode and median are the three measures of central tendency. When modelling a normal distribution large outliers could skew the mean far from the centre thus making a median choice more applicable in some cases. Right / Left skewed curves apply accordingly depending on the mean's position about the median.

2.5.1 Analysis of Variance (ANOVA)

Analysis of variance (ANOVA) is a statistical method that identifies variations between measurements. Interpretations from the table provide information about relationship existences between variables, identifying significant factors and interactions. Different data sets can be tested at different levels. Consequently, this analysis predicts the influence of different factors on one another. A Polymerase Chain Reaction (PCR) can be obtained by dividing the Sum of Squares (SS) distribution over its total value. And an F-ratio is determined by dividing the mean squares over the Degrees of Freedom (DoF). A chosen one, two, or three-way tests are conducted by researchers to evaluate the impact of their studies.

For an ANOVA test to be evident and draw real conclusions off the table, a normal type distribution should be expected from the set samples. In addition to proof that enough data is present to show a high level of significance (P-value). Also, an alternative and null hypothesis must be set, to decide whether to reject the null hypothesis based on a certain confidence interval level. For the reason of set confidence values lying in range (95 – 99%), a Type 1 error may still be present if the null hypothesis has shown to be true. An error term in the table shows residual variables produced using the statistical or mathematical model and does not fully represent the actual relationship between related variables.

2.5.2 Correlations

Regressions are used to predict values about a detected pattern, the closer the value is to the regression line the better it is. Correlations range from -1 to 1, in which 1 and -1 correspond to perfect direct and inverse correlation respectively. Otherwise, a zero value provides no correlation and thus verifies that points are of set randomness. In Mean Absolute Error (MAE), absolute regressions values are added, On the contrary, Mean Squared Error (MSE) values are

first squared then added. Then, both are divided by the number of samples. Both MSE and MAE are used to test correlation correctness, however, It is more applicable to use MSE as it gives more weight to larger outliners, making it a better weigh for the measurement goodness.

Correlation Coefficients describe how well the regression line performs but does not explain its steepness. For Pearson's correlation based on an MAE value, if a p-value is greater than 0.05 for a set confidence interval of 95% the correlation is said to be insignificant. In all correlations, increasing the sample size reduces standard deviation and thus cause a smaller error. Similarly, Spearman's correlation study is conducted using Root Mean Square Error (RMSE) to measure the degree of association between variables, which is less restrictive than that of a linear Pearson correlation.

Chapter 3

Procedure

3.1 Experimental Methodology

3.1.1 Plastic Surface Deformation

In reference to TalySurf's manufacturer's data shown in Figure 2.6, the stylus was attached to a tungsten carbide hemispherical tip of radius R = 0.4 µm, Young's Modulus (E = 700 GPa), and $\nu = 0.22$ (Greaves et al. 2011), pressed against a surface with a force of $w = 10^{-6}$ N.

A Scenario when the tip is in contact with an AlSi10Mg Aluminium alloy surface with a Poisson's ratio tested at 0.37 (Lees et al. 1991), and hardness of 119 HB (400 MPa). Considering the following measurements it has been checked whether the stylus would plastically deform the surface or not, and therefore, calculate the approximate range of scratches if plastically formed.

Since the contact is between a hemispherical tip and a plain flat surface (infinite radius of curvature), circular point contact with a radius of relative curvature R = 0.4 µm is present.

Hence, its reduced elastic modulus is calculated using Equation 3.1:

$$\frac{2}{E'} = \frac{1 - v_1^2}{E_1} + \frac{1 - v_2^2}{E_2} \tag{3.1}$$

$$= \frac{1 - 0.37^2}{75 \times 10^9} + \frac{1 - 0.22^2}{700 \times 10^9}$$

$$E' = 155.4GPa$$

Considering whether plastic deformation would occur at the point of contact, values of load at the onset of plastic yield (w_o) and w_c has been found in terms of hardness (P_p):

$$Y = \frac{P_p}{2.7} \tag{3.2}$$

Substituting in the Radius (R = 0.4×10^{-6}), Reduced Young's Modulus ($E' = 155.4 \times 10^9$), and Y from Equation 3.2 to determine the w_o in Equation 3.3:

$$w_o = 87.9\left(\frac{R}{E'}\right)^2 Y^3 \tag{3.3}$$

$$w_o = 87.9\left(\frac{4 \times 10^{-7}}{155.4 \times 10^9}\right)^2 \left(\frac{P_p}{2.7}\right)^3$$

$$= 2.96 \times 10^{-35} \times P_p^3$$

Similarly substituting the values into Equation 3.4 to calculate for w_c:

$$w_c = 70\left(\frac{R}{E'}\right)^2 P_p^3 \tag{3.4}$$

$$w_c = 70\left(\frac{4 \times 10^{-7}}{155.4 \times 10^9}\right)^2 P_p^3$$

$$= 4.64 \times 10^{-34} \times P_p^3$$

Noting that the factors 2.96×10^{-35} and 4.64×10^{-34} have units of $\frac{m^6}{N^2}$. When multiplied by P_p^3 the product is a force with unit of Newton.

Substituting in the hardness sample value ($P_p = 400 \times 10^6 N/mm^2$) into w_o and w_c:

$$w_o = 1.89 \times 10^{-9}, w_c = 2.70 \times 10^{-8}$$

Hence, the subjected load (10^{-6} N) is 37 times the critical load w_c, so the contact would absolutely be fully plastic, where a scratch mark is left on the specimen.

For fully plastic conditions $w = \pi a^2 \times P_p$, rearranging into Equation 3.5:

$$a_p = \sqrt{\frac{w}{\pi P_p}} \tag{3.5}$$

Substituting values in:

$$= \sqrt{\frac{10^{-6}}{400 \times 10^6 \times \pi}} = \frac{5.642 \times 10^{-4}}{\sqrt{400 \times 10^6}}$$

A circular contact radius $a_p = 2.82 \times 10^{-8}$ is formed. Thus, the tip is approximated to leave a scratch of 0.056 µm wide on the Aluminium surface.

3.1.2 Optical Profilometer Choice

Figure 3.1: S neox, 3D Optical Profilometer – (Sensofar Manufacturers 2021).

Commercially mechanical contact methods are useful, practical small tools matured enough of research and development. AlSi10Mg can be accurately measured with the following contact method, leaving a minor 0.056 µm wide damage on the specimen. This concludes the fact that the following method is ideal for high precision rapid manufacturing components with higher hardness magnitudes providing an excellent measurement and contour topography of the surface finish. On the other hand, for applications that require testing completion without scratches (not entering the plastic region), a TalySurf is still applicable with an appropriate choice of the stylus's radius top and contact force applied.

Mainly, an optical method was preferred over a mechanical stylus because of its simplicity in extracting surface areal parameters providing a whole complete surface representation, as it provides an actual visualisation of the maximum and minimum surface roughness parameters (R_a, R_q, R_{sk}, R_{ku}, R_p, Rv, and R_z) obtained at any plane cutting through the areal surface. On the contrary, the optical method's high-cost form a disadvantage, in this case, standardization

was the main concern as different stitching methods were implemented and exposure settings varied. Smoothing settings and overlapping testing were also employed to achieve precise and accurate readings. Besides, its restrictions in measuring vertical surfaces; as it is difficult to strike vertically downwards light on the specimen.

Repeatability is defined as the test variation obtained by repeating the same sample, with the same measuring equipment, variables, and conditions. This attempts to induce closeness of agreement between the results of the following successive measurements. Testing the repeatability in the Profilometer was not of concern in this experiment, as it had already been tested and calibrated by the Sensofar manufacturers before commercial selling. However, in an attempt to predict the most appropriate option that captures optical images above a 95% set threshold, multiple stitched measurements were repeated, and corresponding light, dull-controls, toolsets, overlapping, and exposure time controls have been tested to obtain optimum settings and base the rest of the work upon.

3.1.3 Design of Experiment (DoE)

Additive Manufactured cubes were fabricated via Laser-based Powder Bed Fusion (LPBF) process using gas-atomized AlSi10Mg metallic powders based on drawn conclusions from section 2.2. An average powder particle diameter in a range of 40 – 60 µm has been estimated. Metallic powders were dried in ovens at a temperature of 343 Kelvin (70°) for 4h then used. Following a 67° laser scanning strategy in Renishaw AM250.

It has been proved that island size does not cause a difference in roughness and porosity outcomes (Kempen et al. 2011). SLM's surface quality is mostly affected by the component's fundamental and derived properties such as point distance, exposure time, laser power, layer thickness, hatch distance, scanning speed, and energy density. Laser power's influence on aluminium alloy surfaces was investigated and it has been persuaded use of laser power value below 340 Watt (Strano et al. 2013); laser powers above this threshold worsens the surface quality associated with an increase in laser beam intensity (see section 2.3.2).

In reference to raw data attached in Appendix B.2, laser power and layer thickness have been fixed to 200 W and 35 µm respectively, leaving three independent parameters to control the outcome. Point Distance (P_D), varying between two consecutive laser beam spots along the scanning line, exposure time (E_T), and hatch spacing (H_S), defined as the parallel distance between laser scans. The three independent variables were analysed, each with its ranging levels detailed in table 3.1; 15 samples in the middle level and 6 on each low and high end to obtain a normal distribution look. Thus, 27 samples were produced to cover all possible combinations contributing to the derived scan speed (v) and energy density (ϕ) quantities.

Table 3.1: Independent variables variation with different levels.

Fundamental Variables	Levels	N
P_D	60	6
	80	15
	100	6
H_S	60	6
	80	15
	100	6
E_T	105	6
	140	15
	175	6

Time consumed by the SLM process is divided into both primary and auxiliary time; primary time required for melting the powder layer and auxiliary for substrate lowering and powder deposition. Exposure time is referred to how long a laser beam strikes on a point; not including auxiliary, nor the laser's reaction movement time. Consequently, the scan speed can be calculated as shown in Equation 3.6:

$$v = \frac{P_D}{E_T} \tag{3.6}$$

3.1.4 Roughness Measurements

All samples top face surface roughness had been measured, and an area of 4×4.8 mm rectangle was to be processed from the total 10 mm^2 top area to minimise possible errors that may affect readings near sides and corners. As a result of the Field of View (FoV) limitation, nine stitched optical images were measured to cover the whole rectangular area with the dimensions shown in Figure 3.2 with a 0.1 mm overlap between neighbouring measurement as illustrated in Figure 3.3:

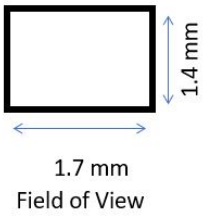

Figure 3.2: FoV Limitation.

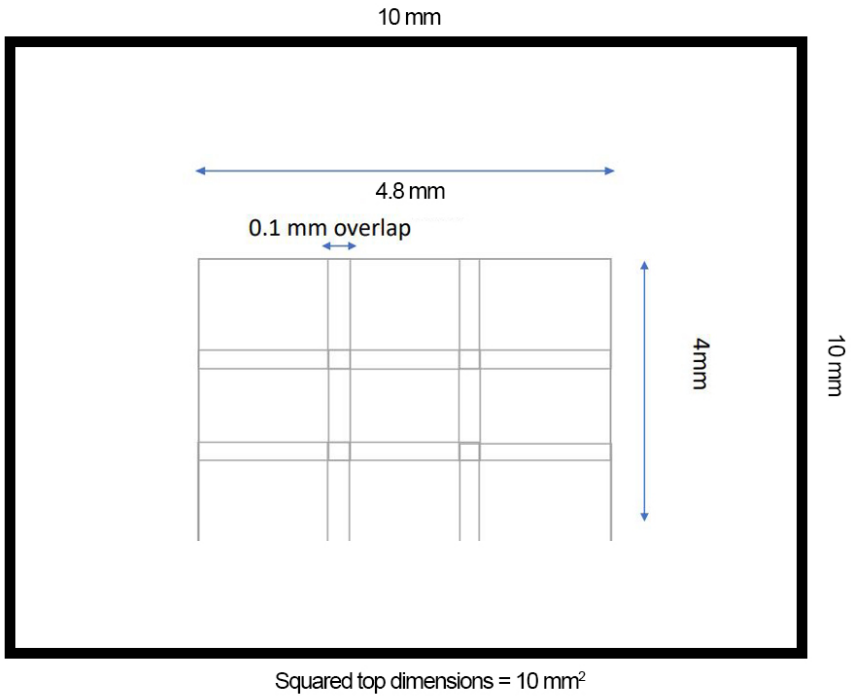

Figure 3.3: Nine stitched images with 0.1 mm overlapping.

Samples were cleaned beforehand, to avoid undesired foreign bodies on the surface as shown in Figure 3.4. Ring light had been placed and tightened and measurements were taken from an initial position. Lens was set out of focus; both upward and downward directions to account for

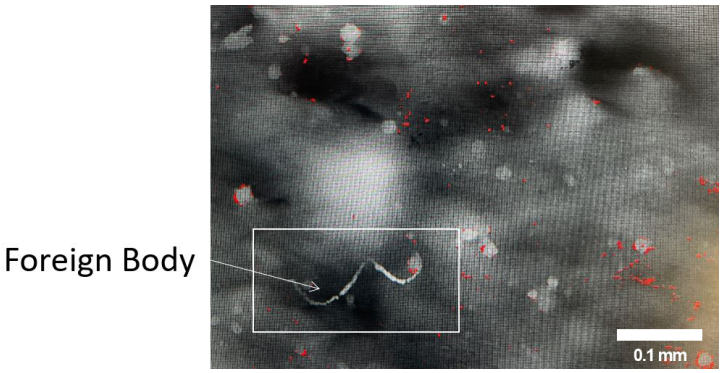

Figure 3.4: A sample's top surface under a 10× optical lens.

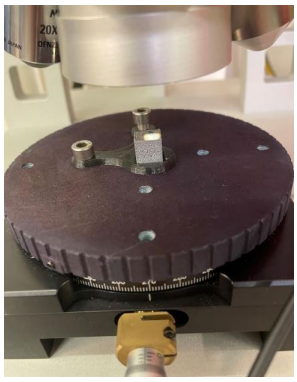

Figure 3.5: Micrometer Control off the Sensofar Profilometer.

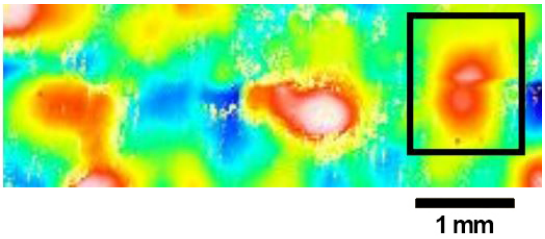

Figure 3.6: Overlapping failure.

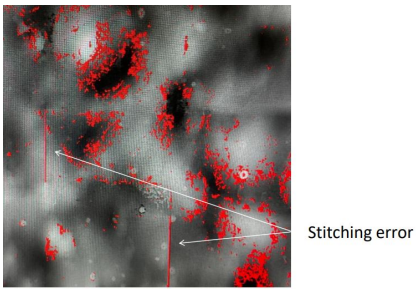

Figure 3.7: Poor measurement and stitching example.

all peaks in the S_z's measurement. Readings were collected from an initial point and between each measurement, the stage was moved by 1.6 mm along X and/or 1.3 mm along Y -axis using micrometre control shown in Figure 3.5 accounting for the overlapping previously discussed.

Processing and Stitching Errors

Stitching values were based on laser scanning boundary analysis; multiple samples have been tested for stitching to maintain the boundary continuity as shown in Figure 3.8 (b). Where high overlapping percentage present in Figure 3.8 (a) and 3.6 were aimed to be avoided. Hence, a studiable stitching pre-set has been programmed based on the overlapping analysis, resulting in a moderate 12% gradient overlapping between neighbouring measurements. Figure 3.7 illustrates another example of a poor measurement that failed in stitching; shown from the vertical unmeasured lines. A high percentage of red unmeasured points arose exceeding 5%. Some lighting problems such as the brightness were non uniformly varied during testing, noticed in dark stitched area boundaries. Thus, all nine images of the following specimen were remeasured and stitched again.

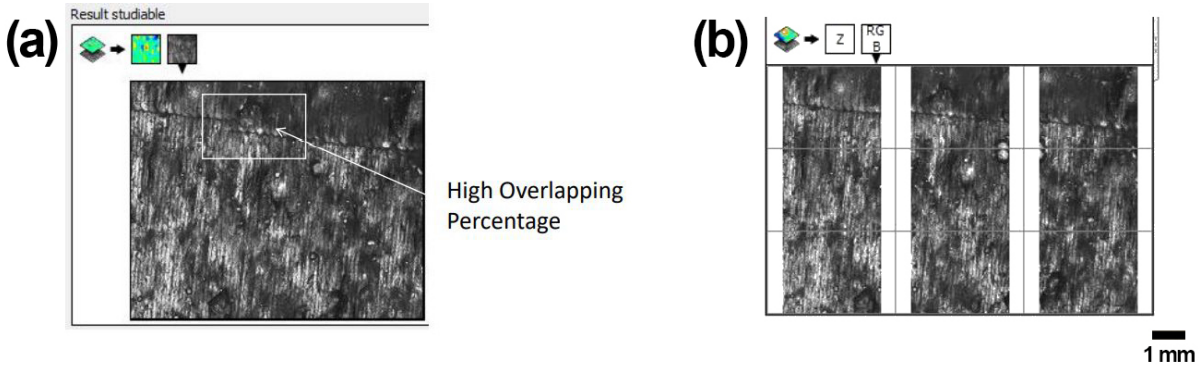

Figure 3.8: Represents a) stitching failure, b) continuous laser boundary travel.

In the current study, the information shows how the topographical data-set process varies considerably and cannot be automated. Through the use of trial and error and scientific testing, it had been deduced that findings could be improved with an increased awareness of data processing steps.

Image Filtering

Image filtration, thus, roughness areal parameter extraction has been tested on a sample, then set to stitch the rest of the measurements as follows:

1. Non-Measured Points were filled using a smooth interpolation
2. S-Filter was applied to remove micro-roughness caused due to measurement system noise.
3. Waviness surfaces, standard filter operator using a 0.8mm Robust Gaussian was selected and surface ends were hence removed.
4. Nesting filter length index set to 2.5 µm, followed by an F-Operator for form removal.
5. Low Filter was applied to separate form, waviness, and roughness parameters of interest.
6. A template was set and the steps had been automatically processed and exported as CSV data files for the rest of the samples.

A sampled work for the highest S_z roughness parameter (367.27 µm) is shown in Figure 3.9 bottom left corner, images were stitched perfectly, then all discussed filters were applied, from (a) to (d), and a final filtered roughness topography had been displayed in Figure 3.9 (e).

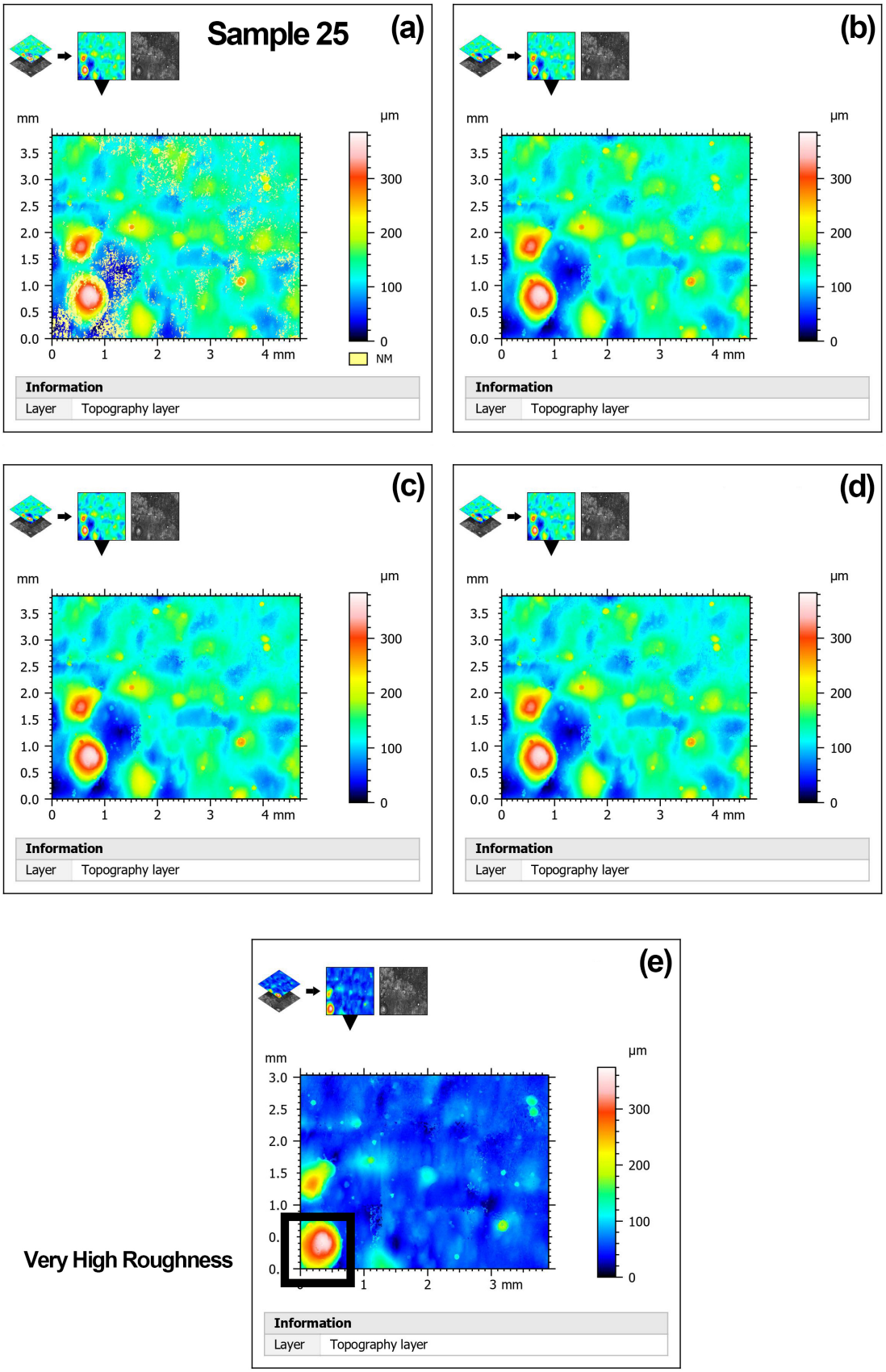

Figure 3.9: a) Initial measurement b) filled in non - measured points, c) levelled (least squares method), d) waviness (Robust Gaussian filer 0.0025 mm applied), e) roughness (Robust Gaussian filter, 0.800 mm).

3.1.5 Porosity Measurements

Samples have been sectioned vertically and horizontally as of their built direction exposing transverse and longitudinal porosities for analysis as illustrated in Figure 3.10.

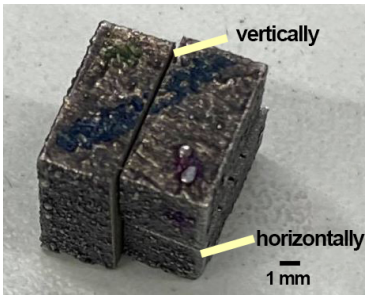

Figure 3.10: Sectioned specimen.

Table 3.2: Grinding and Polishing Experimetal Procedure.

Step No.	Base Surface	Abrasive/Size	Base Speed (RPM)	Direction of rotation	Time (min)
1	Abrasive disc	SiC Paper - P240 (water cooled)	240	Complimentary	10
2	Abrasive disc	SiC Paper - P400 (water cooled)	240	Complimentary	8
3	Polishing Cloth	6 µm Diamond Suspension	120	Complimentary	5
4	Polishing Cloth	3 µm Diamond Suspension	120	Complimentary	5
5	Micro Polishing Cloth	$\sim$ 0.06 µm Colloidal Silica Polishing Gel	120	Contradictory	10

* All polishing steps has been conducted under constant forcing load.

Samples were mounted in thermoset Bakelite plastic, heated in the Struers Mounting Press for 6 min, then cooled for a further 4 min. Subsequently, polishing steps in Table 3.2 were followed. An example of a polish difference from SiC to Diamond Suspension has been clarified in Figure 3.11.

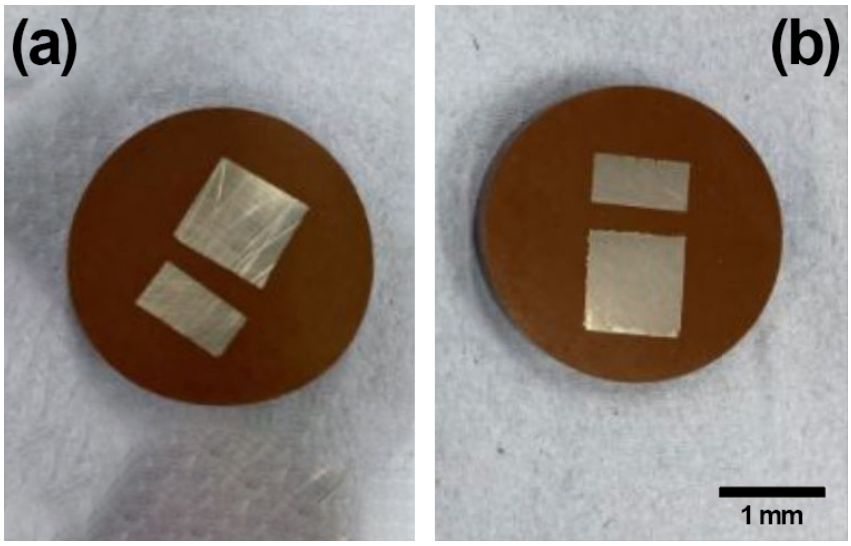

Figure 3.11: Sample took a) before 6 µm and 3 µm Diamond polishing, b) after 3 µm Diamond polishing.

For the porosity measurements to cover a maximum areal measurement, a 5× was chosen over the 50× magnifying lens. Marking all top left, top right, bottom left, and bottom Right corner readings on the microscope for longitudinal porosity measurement as shown in Figure 3.12, taking into account that images projected on the screen are mirrored. In addition to two top and bottom points exposing the transverse side for the horizontal section.

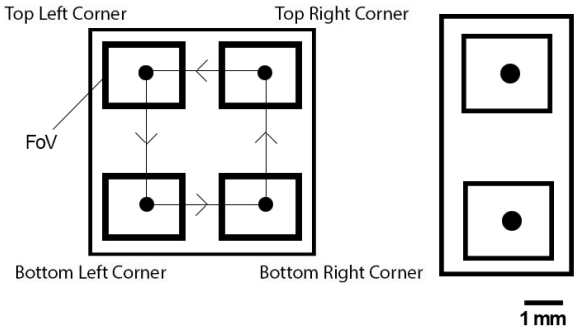

Figure 3.12: Porosity sample measurement.

Figure 3.13 shows three porosity measurements of different samples under a microscope that required re-polishing as scratching errors would account for the pores calculated percentage. Whereas Figure 3.14, shows a straight, thin line from top to bottom revealing a scratch mark arising during polishing that can be accounted for removal in Morphological Image Processing. However, the other large thick black patch at the bottom right side identifies an irregularly shaped void pore that needs to be considered in the porosity measurement.

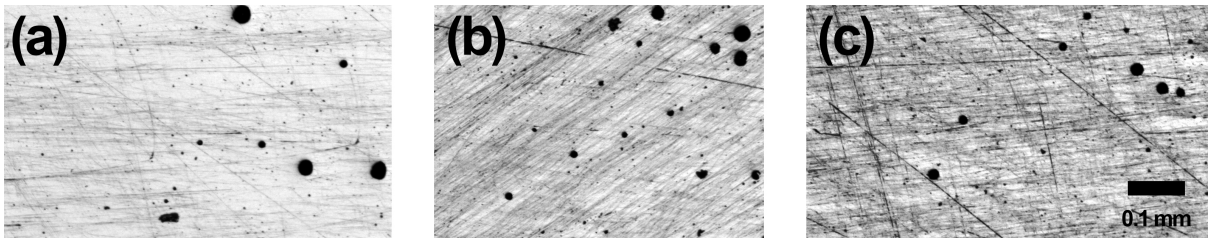

Figure 3.13: a) Scratches in need for silica re-polishing to get diminished (Sample 11), b & c) require a rougher diamond suspension followed by silica re-polishing step.

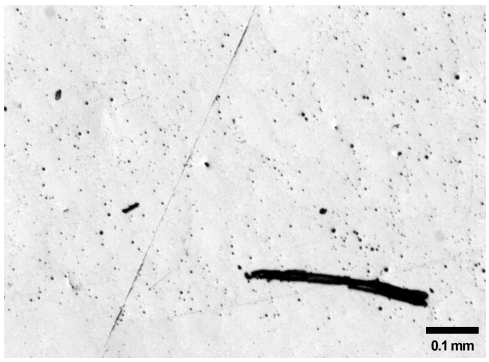

Figure 3.14: Thin scratch line and void porosity (Sample 19).

Morphological Image Processing

A single image was grey scaled (converted into 8-bit) and cropped to standard image dimensions. Afterwards, contrast and auto-tone levelling were applied to the total of 162 images; six for each sample as previously shown in Figure 3.12. Using ImageJ, a threshold has been set and porosity has been determined from the ratio of white to black pixels. The procedure was repeated for all specimens and a mean value for each direction was calculated.

A verification method has been conducted using MATLAB, in which images were loaded into two-dimensional arrays and normalised, kernel matrix size of ones (8×8) was applied to dilate the white pixels and hence erode to maintain the pore sizes after removing fine scratches as the example shown in Figure 3.14. A convolute filter (mean value) of a 9×9 matrix was used to filter out noisy pixels, followed by a threshold value of 0.39 set to convert lower values into black pixels and the rest of polished areas into white. Hence, porosity percentage has been calculated from the ratio confirming data found using ImageJ.

* Details are available for possible reproducibility reasons.

The highest, mean and lowest porosity examples were shown in Figure 3.15 to give a clear scale understanding of the porosity values ranging from 0.76 – 5.57%, an alternative inverted image was displayed for better small pore visualisation as seen in figure 3.16. The cross-sectioned particles revealed the internal structure of the powder and correspond to the presence of trapped gases contributing to porosity in the bulk produced samples.

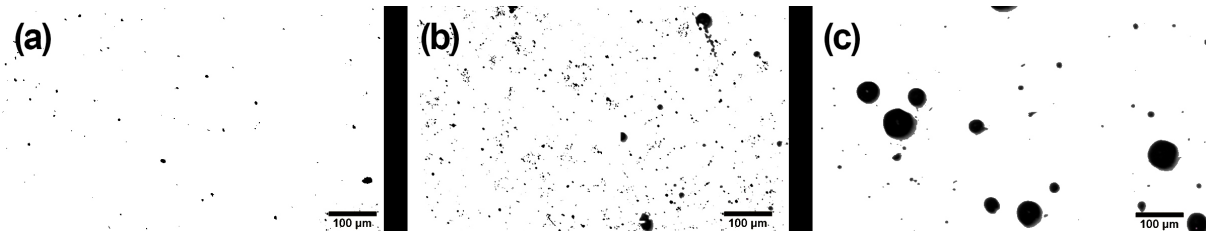

Figure 3.15: An example of a transverse a) lowest porosity (Sample 13: 0.76%), b) mean porosity (Sample 1: 1.63%), c) highest porosity (Sample 18: 5.57%).

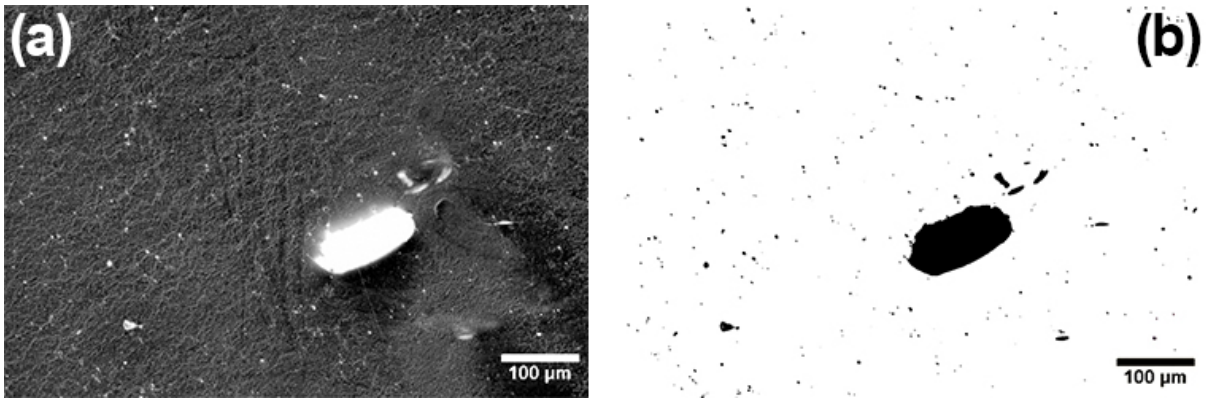

Figure 3.16: For small pores better visualisation, final image representation were either a) inverted, b) non-inverted image.

Chapter 4

Results and Discussion

4.1 Roughness

4.1.1 Data Processing

Table 4.1: Lowest Areal Roughness Measurements Against Manufacturing Parameters.

	$S_a/\mu m$	$S_q/\mu m$	$S_z/\mu m$	Manufacturing Parameters
Sample 18	6.81	10.56	150.46	$E_T = 140$, $P_D = 60$ and $H_S = 100$
Sample 26	6.45	9.31	157.02	$E_T = 140$, $P_D = 80$, and $H_S = 80$
Sample 17	8.73	13.52	190.02	$E_T = 140$, $P_D = 100$, and $H_S = 60$

The lowest three roughness measurements shown in Table 4.1 varied combinations of either 60 & 100, or 80 & 80 P_D and H_S values respectively; which means that if hatch spacing between scanning lines is highest (100) the lowest distance between each laser beam strike is required to achieve a minimum surface roughness and vice versa. Meanwhile, the medium H_S along with P_D level would also provide low roughness values.

S_a and S_q values have been plotted against the sample numbers shown in Figure 4.1. Further clarification using Wilcoxon's Signed Rank Test has been illustrated in Figure 4.2 (b), and proved that all S_q values are of positive differences to S_a, with a significance value of 0.0006 calculated in the non-parametric test, which proves the measurement's reliability as S_q results from the root mean square average of height deviation taken from the mean image data plane.

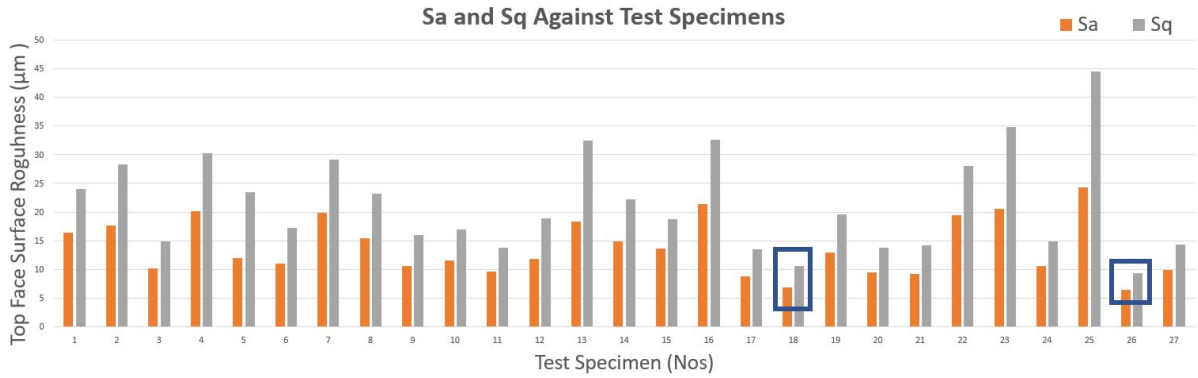

Figure 4.1: Minimum roughness values in Sample 18 and 26.

Based on conclusions in subsection 2.4.1, S_a, S_q and S_z are adequate output parameters to be considered out of all obtained aerial roughness parameters. In Figure 4.2 (a), an additional S_z parameter has been added to the comparison on a logarithmic y-axis plot. S_z's Box and Whisker represented maximum range and thus maximum Inter-quartile Range (IQR) of 111.5 leading to the largest value spread corresponding from the maximum range of S_p previously illustrated in Equation 2.3.

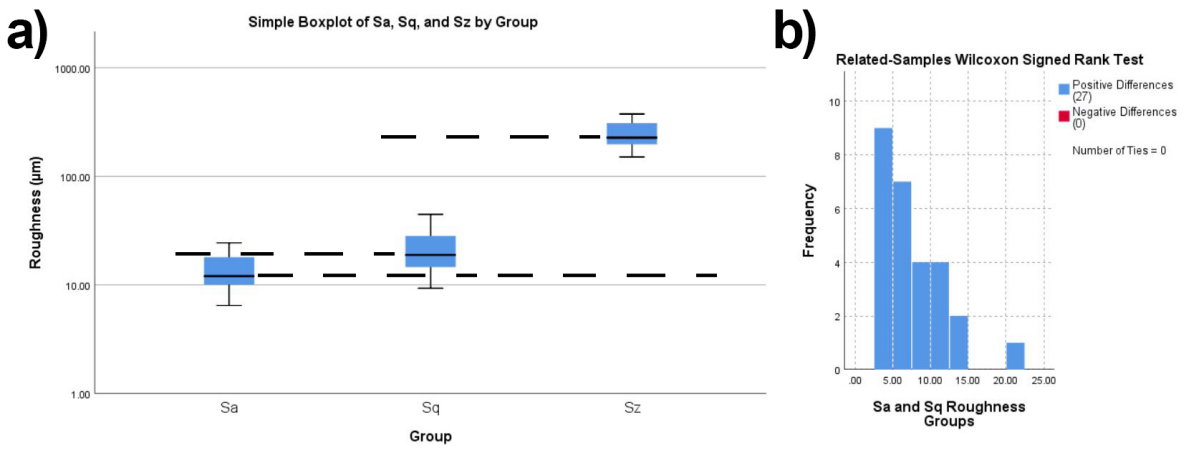

Figure 4.2: a) Box and Whisker plot identifying IQR, b) Showing a significance in positive differences between S_a and S_q.

Since S_a's mean and median values presented a 1.2% right skewness between centres, thus both values would provide a good normal distribution central tendency point for set analysis. Roughness against segregated scan speed results has been plotted in Figure 4.3, where all three S_a, S_q and S_z plots have shown similar box minimums. And since v is a derived parameter influenced by two of the three independent variables (P_D and E_T) as shown in Equation 3.6. Based on this valid dependence it has been shown that minimum median values lied under 428.6 and 761.9 mms $^{-1}$ segregated points in all three areal measurements.

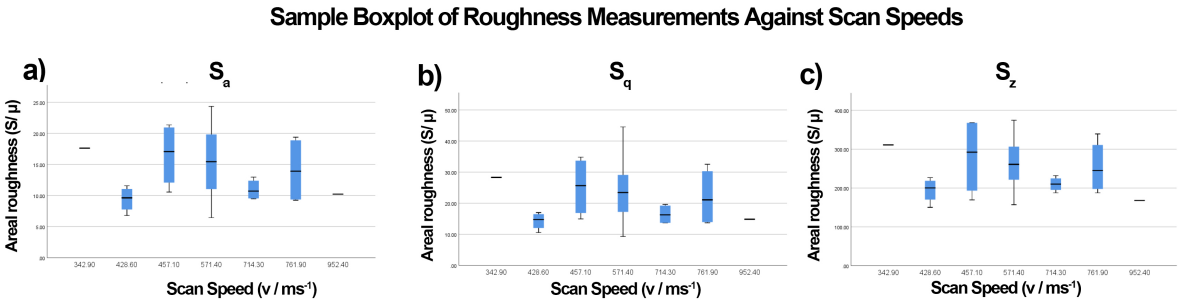

Figure 4.3: Areal roughness measurements plotted against segregated scan speed values verifying minimums values under 428.6 and 761.9 mms $^{-1}$

Illustrating testing of S_a against ϕ in Figure 4.4 (b), the described data assigns the lowest roughness with multiple points above it under the same energy density, thus shifting the mean graph upwards as shown in the figure 4.4 (a) resulting into wrong data interpretation if the following visualisation has been followed. Thus, since both (v and ϕ) influence the roughness output as their equations are affected by the experiment's fundamental parameters, a minimum S_a value with different combinations of energy density and scan speed has been plotted in Figure 4.5. The following 3D plot displayed a roughness against both derived parameters. Where a minimum value ($S_a = 6.45$ µm) corresponding to Sample 18 pointed at using the blue arrow previously displayed in Table 4.1

However, it can still be seen that several readings within a small variation of ϕ and v lie above the point, and hence the output variable is neither a simple function of scan speed on its own nor just the two derived quantities.

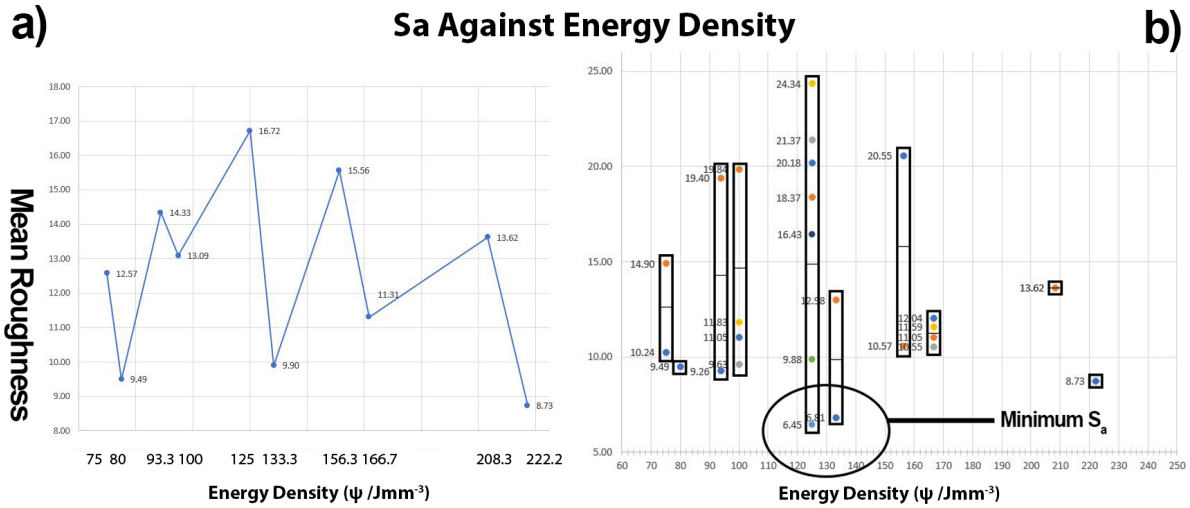

Figure 4.4: a) Mean roughness plot against ϕ, b) All point plots verifying the wrong choice of mean line plot

Minimum values of energy density ranged closely $125 - 133.3$ (3.7% difference) as shown in Figure 4.5, and scanning speed ranged correspondingly marking an 8.5% difference from the red (second-lowest roughness value) to the blue arrow.

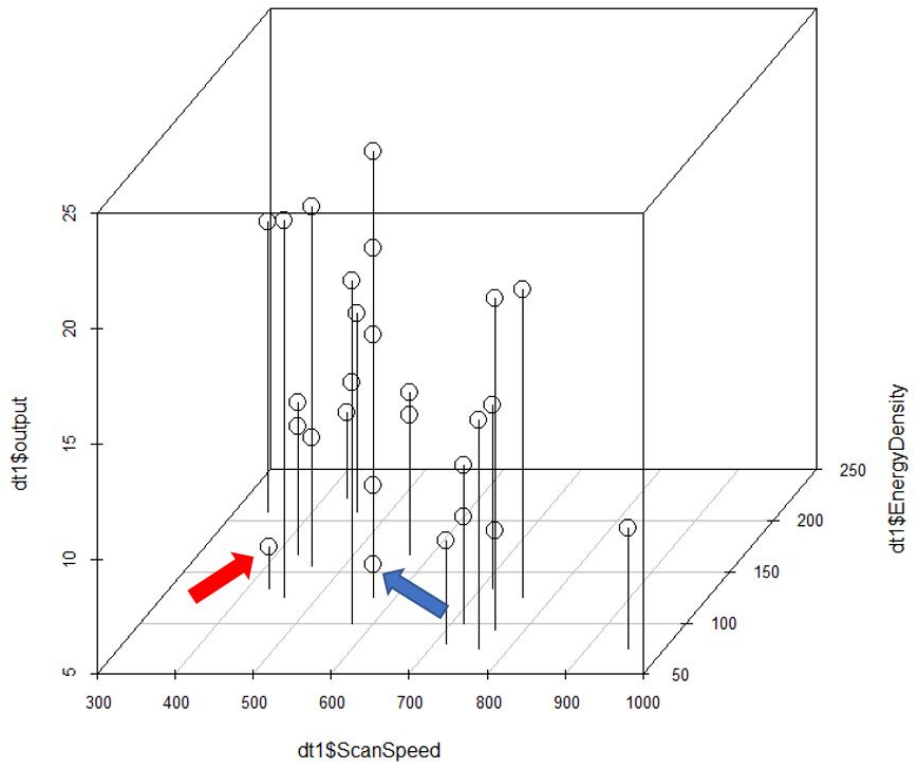

Figure 4.5: Lowest two S_a values has been marked in blue and red arrows, expressed in a 3D plot against energy density and scan speed.

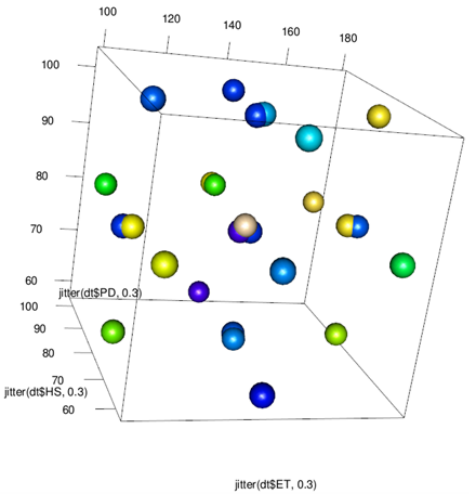

Figure 4.6: S_a against inputted parameters (P_D, E_T and H_S).

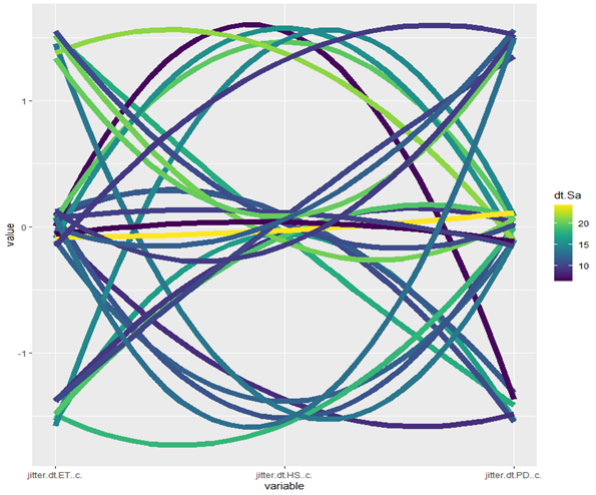

Figure 4.7: S_a against inputted parameters in a parallel coordinates plot.

A primary goal of a physical representation is to determine the interaction between the three variables. Thus, data has been also plotted as follows using another 3D plot in Figure 4.6. The dependent (S_a) coloured the points with topographical colouring; where colours range from deep violet, with the smallest values to deep blue, green, yellow, and light brown being the highest value.

The deepest violet, and hence lowest S_a values lied more or less in the middle of the cube, but the following points also coincide with the highest roughness value being one of the three central ones. Hence, the settings which produce very low values result in the highest one! Therefore, the following main plots are also insufficient to locate the minimum value. Another parallel coordinates plot has expressed the same data differently in Figure 4.7. Each of the experiments was shown as a curved line joining the set values of P_D, E_T and H_S similarly coloured by S_a. The highest and lowest cases of S_a are in the middle of the plot and still unclear to interpret.

ANOVA Testing

Regression with dummy variables does not consider the fact that variables have directions. Hence, fixing the variable P_D as shown in Figure 4.8, and testing the interactions using a two-way ANOVA would eventually lead to incorrect analysis. Thus, a three-way test has to be tested against the dependent variable (S_a) as shown in Table 4.2.

Point Distance	Exposure time			Hatch Spacing		
Low	16.43256	10.55143	17.62676	8.73195	16.43256	6.808792
	0	11.58751	0	0	17.62676	0
	0	8.73195	0	0	10.55143	0
	0	6.808792	0	0	11.58751	0
	0	0	0	0	0	0
	0	0	0	0	0	0
	0	0	0	0	0	0
Medium	18.37101	12.03685	13.62221	12.03685	9.264259	19.84161
	14.89662	11.04753	21.37346	11.04753	19.40224	15.44671
	9.264259	19.84161	20.5543	18.37101	20.5543	14.89662
	19.40224	15.44671	10.56787	13.62221	10.56787	21.37346
	0	24.34281	0	0	24.34281	0
	0	6.445746	0	0	6.445746	0
	0	9.875717	0	0	9.875717	0
High	10.24412	9.626431	20.18086	12.98465	10.24412	9.492688
	0	11.83046	0	0	20.18086	0
	0	12.98465	0	0	9.626431	0
	0	9.492688	0	0	11.83046	0
	0	0	0	0	0	0
	0	0	0	0	0	0
	0	0	0	0	0	0

Figure 4.8: S_a values rearranged with fixed P_D (low, medium and high).

Table 4.2: Three-way ANOVA for S_a.

Source	DoF	Sum of Squares	Mean Squares	F-calculated	Significance	PCR
P_D	2	16.69	8.34	0.23	0.8	3.16
H_S	2	0.69	0.34	0.01	0.99	0.13
E_T	2	79.88	39.94	1.08	0.38	15.13
$P_D \times H_S$	4	52.14	13.03	0.35	0.83	9.88
$P_D \times E_T$	4	43.14	10.79	0.29	0.87	8.17
$E_T \times H_S$	4	40.5	10.13	0.27	0.89	7.67
Error	8	294.82	36.85			55.85
Total	26	527.86				100

* Statistically significant at 95% confidence level.

The relationship between the manufacturing performance and processing control parameters can be exposed using ANOVA. The measure utilised the influence of input parameters on the total response variation. From the total number of samples, a total of 26 Degrees of Freedom (DoF) were present. And thus, an additional $P_D \times E_T \times H_S$ three-way interaction was not inputted in Table 4.2 since it adds eight further DoF, creating a fully saturated model with zero error. Consequently, neither an F-value nor a comparison between the sum of squared values with pooled error could be calculated.

Table 4.3: Independent Variable Level Changes.

Variable	Point Distance, P_D / µm	Exposure Time, T_E / µs	Hatch Spacing, H_S/ µm
±	20	35	20
High	100	175	100
Medium	80	140	80
Low	60	105	60

The Sum of squares indicates the following variability and displays it in an ANOVA test. Concerning the measures of dispersion, P_D and H_S's variance is much lower than E_T as their data and thus variance is closely clustered around the mean with a lower ± level difference identified in Table 4.3. It was deduced that the highest PCR was lead from E_T followed by the interaction of $P_D \times H_S$ (PCR = 9.88), all with an insignificant value. What also can be concluded from Table 4.2 that H_S implies the lowest contribution and significance on the result, where its changes would not reach the model. Similarly, S_q and S_z ANOVA tests shown in Appendix B.3 and B.4 also proved that the factors had no significance on one another.

In reference to Table 4.4, all variables expressed positive correlations against S_a, with the highest correlation coefficient in Spearman's rho and Pearson's of 0.214 and 0.177 (moderate values) respectively, confirming that E_T is S_a's highest contributor previously confirmed in Table 4.2. On the other hand, P_d's increase against S_a is significantly low (closest to zero), showing the weakest relationship both using Spearman's and Pearson correlation coefficient assessments, assigning it with a high percentage of data randomness.

Table 4.4: Spearman's and Pearson Correlation Coefficient.

			P_D / µm	T_E / µs	H_S / µm
Spearman's rho	S_a	Correlation Coefficient	0.043	0.2014	0.078
Pearson	S_a		0.030	0.177	0.128
		Sign, (2-tailed) P value	0.832	0.284	0.697

E_T was modelled on a parallel Box plot with all its data variations within assignment against S_a, S_q, and S_z. Accordingly, it has been shown to optimise in Figure 4.9 at $E_T = 140$ where all three roughness parameters are seen to be at the lowest.

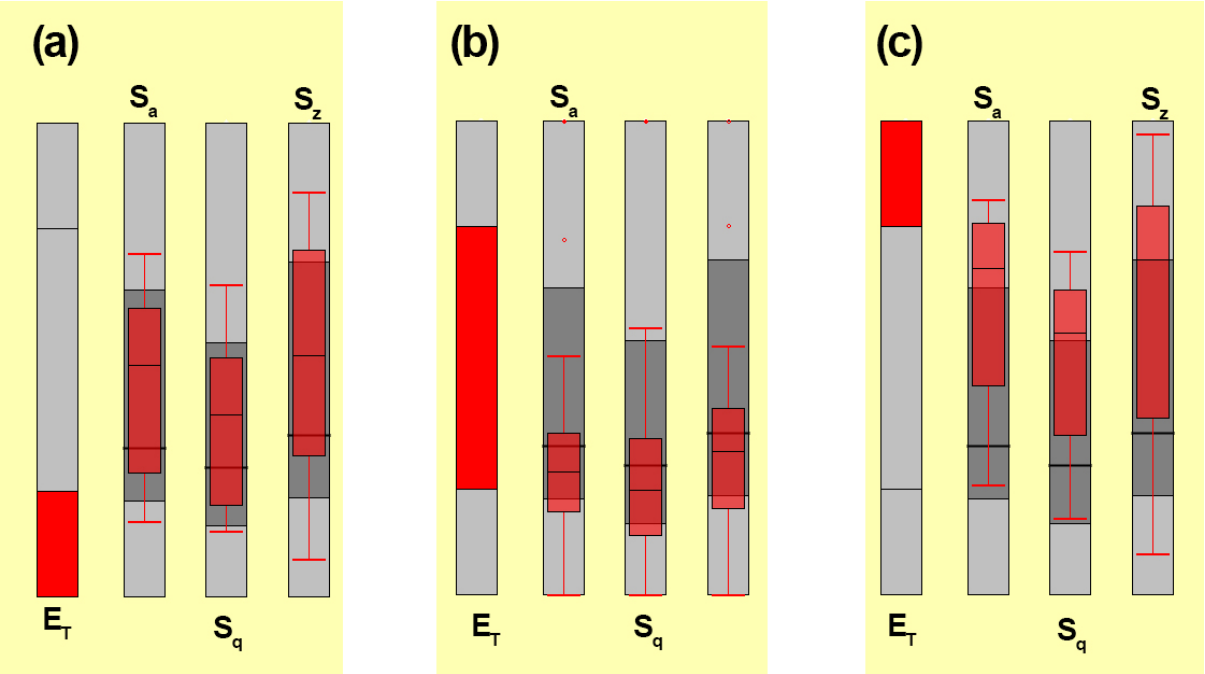

Figure 4.9: A Box plot of a variety of E_T against S_a, S_q, and S_z.

Since the previous graphical representation of the three surface roughness parameters appeared to be similar, thus a plot focusing on S_a's further analysis is adequate on its own. Shown in Figure 4.10, main effect plots of the three independent parameters indicated optimised points under P_D values of 60 & 100, and H_S at 60 noting that its significance is shown to be the lowest from the main plot's middle line gradient confirming on Table 4.2. Finally, E_T was optimised at 140 as previously justified in Figure 4.9.

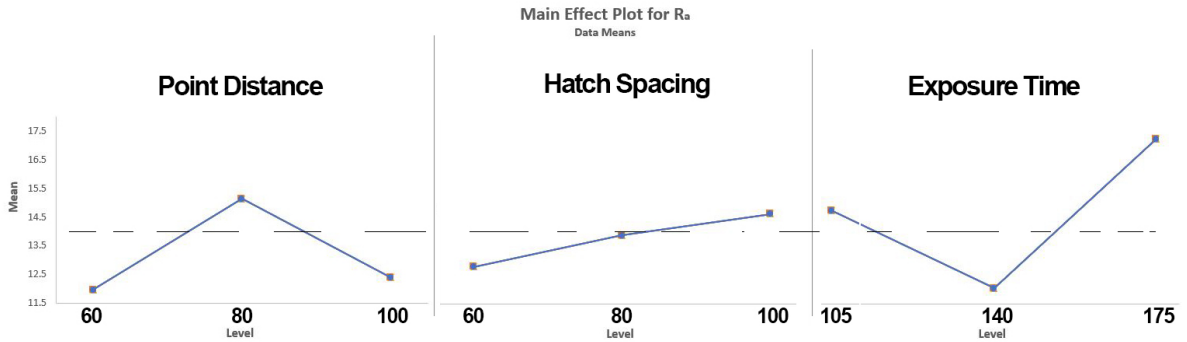

Figure 4.10: Main Effect Plot for R_a against levels proving all optimised variables except P_D.

Since most roughness values were minimum at, $v = 428.6$ and 714.3 ms^{-1} shown in Figure 4.3, thus referring to Equation 2.2, P_D aslo calculates at 60 and 100 respectively, referring to the optimal points in Samples 17 and 18. However since optimised energy densities were verified to lie between $\phi = 125$ – 133.3 Jmm^{-3} in Figure 4.5, and Sample 17 was classified under a single segregated energy density plot ($\phi = 222.2$ Jmm^{-3}), thus its uncertainty of choice error is high, and Sample 18 was chosen instead in which its value optimises under ($\phi = 133.3$ Jmm^{-3}).

4.1.2 Data Interpretation

Reviewed literature emphasised that surface roughness and porosity are mainly affected by the scan speed and energy density. Coloured topography in Figure 4.12 below has shown a uniform roughness in all areas except the top right corner that dragged S_a mean value upwards making Sample 17 the third least measured roughness value instead of least. Due to lack of multiple trials, thus topographies of the same sample, it has been deduced that bowling and saddling effect has shown to have occurred in the red circular region at the top right corner. An explanation for the following is shown from the presence of evaporation and splashings within the melt pool during manufacturing. This lead to a high corner roughness value. Such a result has risen S_p and thus S_z value into 190.02 µm making it 18% higher than the lowest S_z roughness value in sample 18.

The high energy density low scan speed manufacturing combination meant that lower scan speeds are preferred because they permit smoother surfaces through fully melting the powder with a possibility of high S_z values at the corners.

In Figure 4.11, another example of the lowest calculated energy density ($\phi = 75$ Jmm^{-3}) has been demonstrated. In which most points lied closest to the mean roughness indicated in yellow; in reference to the scale bar. The lowest energy density shown in Sample 3 formed unfused, fine-sized metal powders attached to the surface shown in red dots under the influence of high scan speeds, contributing to high roughness values. Possibly, if different independent parameter combinations were investigated, higher energy densities than the ones currently in experimentation would develop, thus multiple values under $\phi = 222.2$ Jmm^{-3} segregated result allows for further analysis on high energy density.

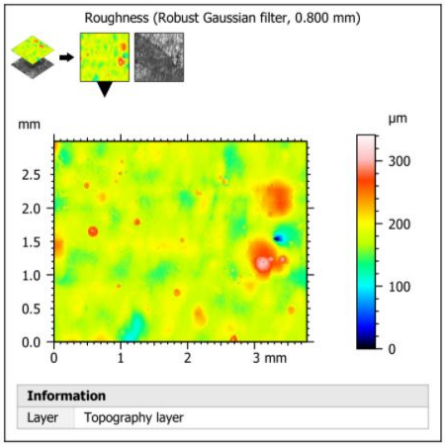

Figure 4.11: Lowest energy density ($\phi = 75$ Jmm^{-3}) on Sample 3.

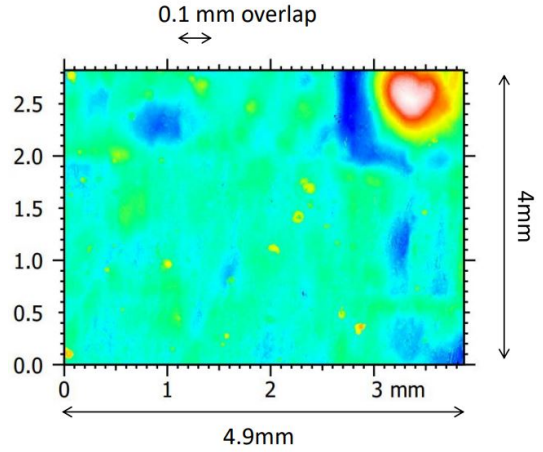

Figure 4.12: Bowling and saddling effect under $\phi = 222.2$ Jmm^{-3} on Sample 17.

4.2 Transverse and Longitudinal Porosities

4.2.1 Data Processing

Porosity percentages have been plotted against the median as shown in Figure 4.13 with present outliers making it more applicable for analysis; as a mean choice would skew the central values showing 20% right-skewed shifted data. As seen in Figure 4.14 (b), a combination of both positive and negative differences within each sample's longitudinal and transverse directional porosity readings provided a p-value of 0.428, thus a low significance of both directional data on one another as their corresponding median values were shown to be crossing each other's IQR, and hence should be interpreted separately.

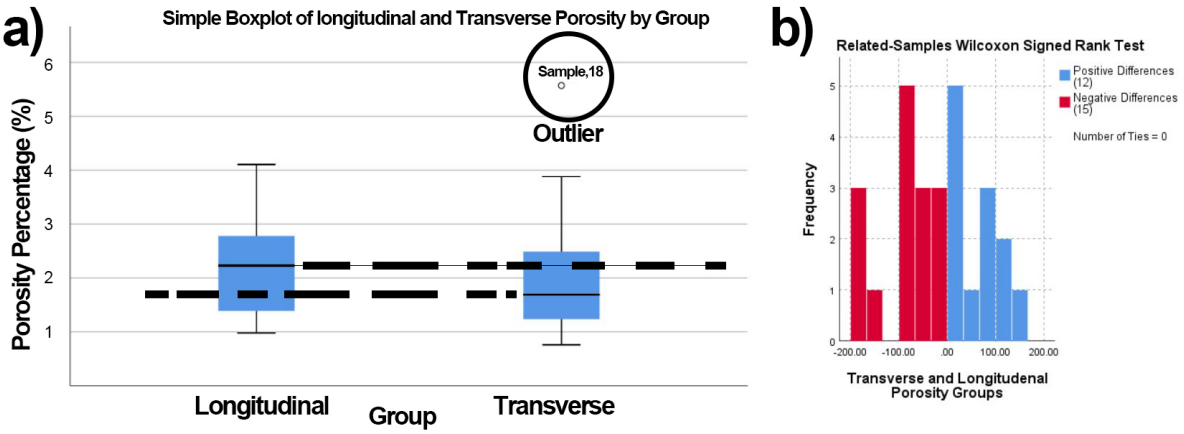

Figure 4.13: a) Box and whisker plot identifying IQR, b) Showing positive and negative differences between longitudinal and transverse porosites.

Table 4.5: Transverse Direction (ANOVA) Three-way result.

Source	DoF	Sum of Squares	Mean Squares	F-calculated	Significance	PCR
P_D	2	3.07	1.54	7.70	0.0136	11.04
H_S	2	4.39	2.19	11.00	0.0048	15.76
E_T	2	1.36	0.68	3.42	0.0847	4.90
$P_D \times H_S$	4	12.91	3.23	16.18	0.0007	46.38
$P_D \times E_T$	4	2.50	0.62	3.13	0.0795	8.97
$E_T \times H_S$	4	2.01	0.50	2.52	0.1238	7.22
Error	8	1.60	0.20			5.73
Total	26	27.84				100

Porosity in transverse direction ANOVA three-way result shown in Table 4.5 marks H_S's interaction with P_D at its highest significance and PCR. This followed by H_S's solely significance, and then P_D also lying within a 95% confidence interval below the set cut-off value ($\alpha = 0.05$). This finding is contrary to the null hypothesis and supports the effect of factors on its small variation. On the other hand, longitudinal ANOVA did not verify any significance as displayed in Appendix Table B.7.

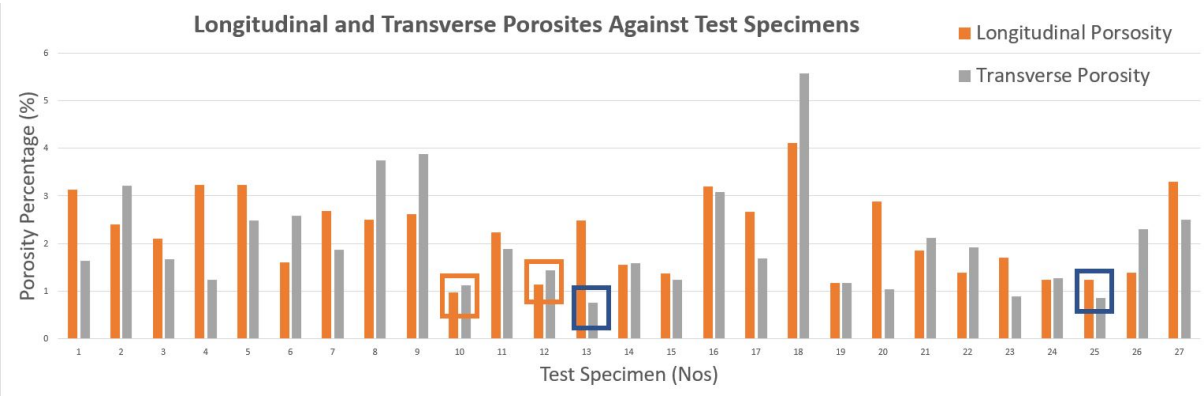

Figure 4.14: High density structures illustrated in rectangles corresponding to raw values in Appendix B.5 and B.6.

Table 4.6: Transverse Direction (ANOVA) Two-way Result.

Source	DoF	Sum of Squares	Mean Squares	F-calculated	Significance	PCR
v	5	12.769	2.554	2.868	0.043	35.54
ϕ	9	12.472	1.559	1.751	0.184	34.72
Error	12	10.685	0.89	3.42	0.0847	29.74
Total	26	35.926				100

Table 4.6 illustrates the influence of scan speed on energy density two-way result. As v is the only term that showed significance within 5%, v's significance has been confirmed from the larger differences within the box plots in Figure 4.16 over 4.17, showing that the scan speed derived quantity is of more significance and importance on the final porosity output. An optimisation between the energy density and the speed of fabrication should be considered for the transverse porosity direction as balling increases with higher scanning speeds as shown in Figure 4.16.

Both main effect porosity measurement plots shown in Figure 4.15, proved an optimised minimum point either at $E_T = 105$ or 175, 60 – 80 for both H_S plots, and complete opposing results and thus line gradients for P_D where longitudinal porosity minimises at 80, and transverse at 100. Hence, an optimum point lies between 80 and 100, but the intersection seemed to tend closer to 80.

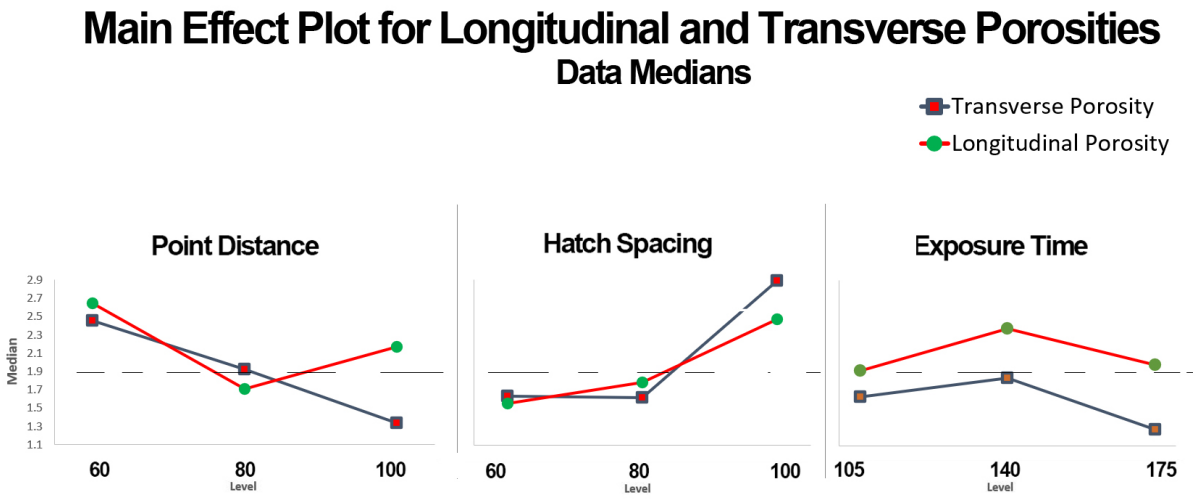

Figure 4.15: Main Effect plot for both porosity types against the independent variables.

Table 4.7: Porosity Optimisation – P_D Calculation.

v/mms^{-1}	E_T/ µs	Calculated P_D/m
457.1	105	48
457.1	175	80
714.3	105	75
714.3	175	125

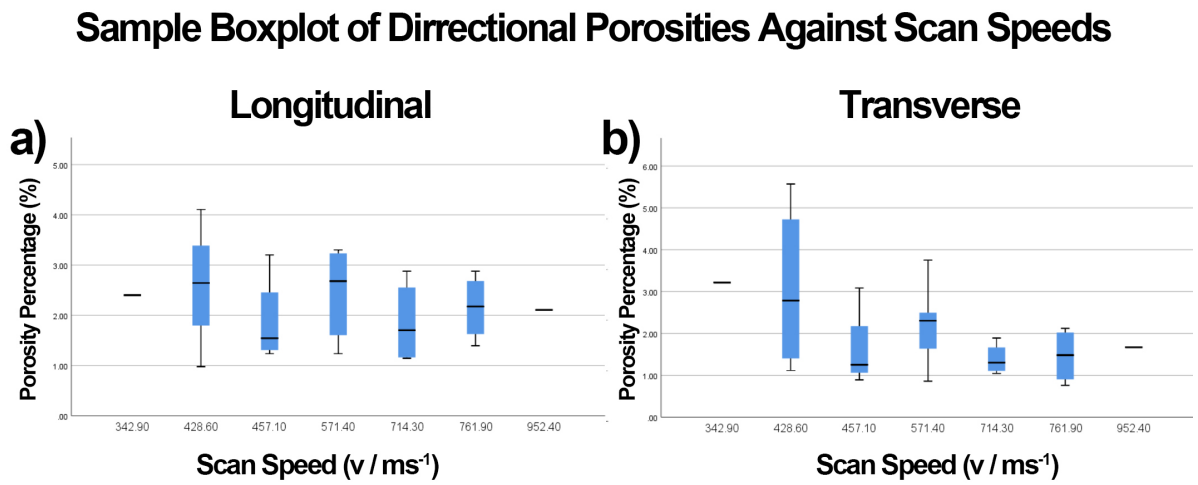

Figure 4.16: a) Longitudinal, b) Transverse porosity percentage plot against v.

When measuring a Box and Whisker plot of both directional porosities for the reason of showing median values, optimal porosity measurement lied under segregated scan speeds of 457.1 and 714.3 mms $^{-1}$. Since minimum porosity occurs at either E_T = 175 or 105 µs, thus, all four combinations has been calculated for P_D through Equation 3.6, illustrated in Table 4.7. Where testings have found that 48 and 125 P_D lied outside the ranged measurement leaving out 80 and 75. And since the intersection line lied closer to 80 then a value of 80 is to be considered as optimised Point Distance.

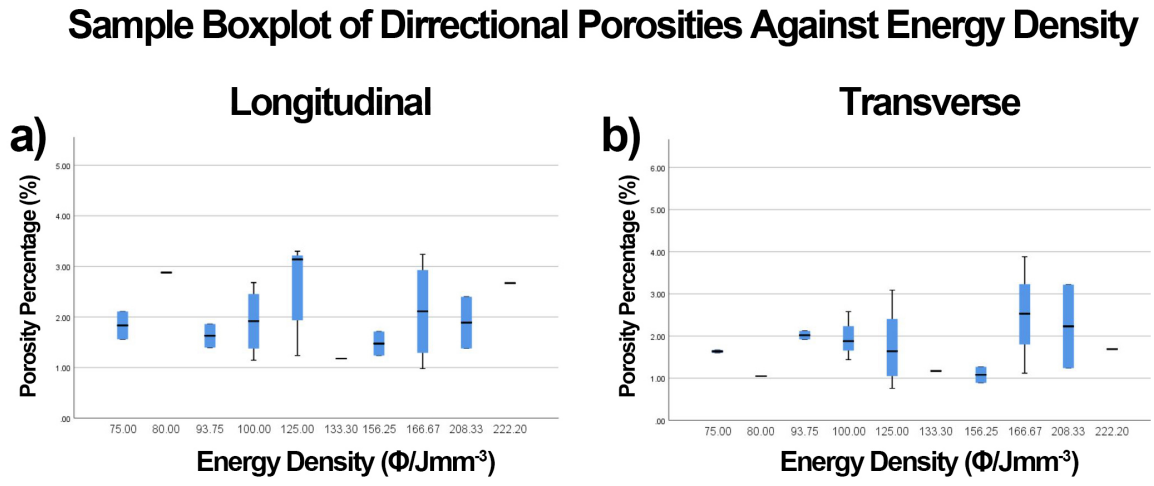

Figure 4.17: a) Longitudinal, b) transverse porosity percentage plot ϕ.

Neglecting outliers in Figure 4.17, as for samples of porosity values tested under a single segregated energy density plot showing high error uncertainty, both optimised directional porosity measurements were found optimal under the segregated plot of 156.25 Jmm^{-3}. Thus, since all E_T's confirmed optimal point at 175 and v = 457.1, along with information of fixed H_S, t, and Power, H_S calculates as 80 µm using Equation 2.2 under Specimen calculation provided in Appendix B.5. Consequently, optimised independent parameters for minimum porosity in both directions optimise as follows in Sample 23:

Table 4.8: Porosity Optimisation – Result Summary.

Sample	Mean Porosity	Manufacturing Parameters	ϕ/Jmm^{-3}	v/mms^{-1}
S23	1.30 %	$E_T = 175$, $P_D = 80$ and $H_S = 80$	156.3	457.1
S10	1.05 %	$E_T = 140$, $P_D = 60$ and $H_S = 80$	166.7	428.6

In reference to Tables of lowest longitudinal and tranverse direction measurements in Appendix B.5 & B.6 respectively, lowest combined longitudinal and transverse mean porosity measurement is to be minimum for sample 10 as outlined in Table 4.8. But since the sample corresponded into v = 428.6 and ϕ = 166.7 Jmm^{-3}, their following porosity measurements lied outside the Box and Whisker plots seem in Figure 4.17 & 4.16 thus making sample 10 appear as an outlier.

4.2.2 Data Interpretation

The results identified pores in SLM-processed samples, governed by the laser beam's scan speed and energy density showing an effect on both longitudinal and transverse directions in Figure 4.17, with a high hatch spacing significance as shown in the three-way transverse direction ANOVA ($H_S = 80$) applied to the lowest porosity measurements in Table 4.8 on both Samples 10 and 23. Where the optimum point in Sample 23 corresponded to the maximum exposure time on each laser spot along with medium point distance and most importantly medium hatch spacing. It has been concluded that slow solidification with high exposure times led to a dense formation where all areas managed to melt consistently. However, for industrial manufacturing, the implementation of sample 10 manufacturing parameters would be considered a better option over sample 23; as the maximum exposure time is too long making the process uneconomically viable for mass production (subsection 2.3.1).

4.3 Errors and Possible Improvements

- The study did not examine any error bars during analysis since roughness optical measurements were stitched together to provide a single whole surface, similarly, a single trial was conducted for porosity measurements and a mean value of all corner readings has been calculated. An increase in the number of data sets experimenting with more samples and measuring multiple trials would establish a greater degree of precision and accuracy.

- Varying three independent parameters on 27 samples lacked a persistence in quadratic minimization as more samples are required; H_S, E_T and P_D failed to fit into a quadratic model based on the AM parameters provided, in order to module an error surface with a minimum, to differentiate the quadratic model and find the interpolated minimum. Also, more quantitative data (samples) would allow the use of other regression models.

- The experiment covered a relatively small scan speed and energy density spans as a result of the small fundamental parameters variation. This could be improved by increasing the levels and their effects on the derived quantities. i.e. higher number of levels for each factor would lead to a wider segregated data outcome. Different combinations of higher independent values would also obtain higher segregated energy density results according to Equation 2.2, thus, allow the experimentation under higher energy densities to check the validity of sample 10's result. After completing the experiment, as it has been determined that all minimum roughness and porosity measurements were contributed under the optimised settings in Table 5.1, therefore, closer variations to the optimised concluded values could be further experimented separately within $\pm$ 5 level differences from both ends attributing into a more accurate optimised conclusion.

- If the porosity study is to be remeasured again, a mechanical polishing procedure in subsection 3.1.5 would be of better practice if a further 1 µm was followed after the 3 µm Diamond Liquid Polish process reducing the likeability of detecting scratches on the surface affecting transverse and longitudinal porosity readings.

- The pixel ratios method to identify pores on the magnified polished samples on its own is not reliable; as shown from the result variation of the same specimen tested from different corners as seen in Appendix B.3. Therefore, better in-depth Morphological Image Processing research and testing should be conducted.

Chapter 5

Conclusions

5.1 Roughness and Porosity Optimisation

Table 5.1: Roughness and Porosity Optimisation – Result Summary.

Optimised	Sample	S_a/ µm	Porosity	Manufacturing Parameters
Roughness	Sample 18	6.81	4.83%	$E_T = 140$, $P_D = 60$ and $H_S = 60$
Porosity	Sample 23	20.55	1.30%	$E_T = 175$, $P_D = 80$ and $H_S = 80$

In summary, the applicability of AlSi10Mg's use in the automotive and aerospace industries is due to its excellent castability and weldability. These properties are essential in manufacturing fully dense and thin layer structures.

Designers have a choice between friction and life expectancy when choosing materials for shafts, bearings, and other functional automotive and aerospace components. Testing the applicability of AlSi10Mg for manufacturing near net shape is still not valid; i.e. shaft applications for cars lie within the range of 32 to 64 rms (0.8 – 1.6µm) that is far less than the outputted optimal surface quality where further post-processing procedures such as mechanical or laser polishing are required. However, in practical applications the smoother the surface is not necessarily the better, it depends on the application; braking examples may require high roughness to provide a better grip on the ground.

In research, roughness and porosity output responses have been optimised separately as parameters optimise differently from roughness to porosity minimums. There are multi-objective optimisation methods that can hence be considered for more than a single output response and further build on this research.

For porosity measurements, transverse directional porosity readings are shown to validate a lower optimal point than longitudinal. Hence, mounting the material on the transverse surface perpendicular to the tensile forces causes yielding at higher limits. It has also been verified from all-optical images that pores were fully enclosed making the manufacturing process safe from leakage suffering in bearing applications. Corresponding to its high nearly fully dense percentage (98.7%) this proves its application in cam covers, inlet manifolds, and throttle bodies. If there has been a need for higher dense values, then a vacuum impregnation could be subject to permanently seal porosity ranging from 0.5nm to 100nm in automotive castings. This is carried out by a piece of equipment that draws air out, enabling the formulated resin to fill gaps within the casting.

Keyhole pores enclose non-molten powder parameter-dependent formations. When increasing scan speed, irregularities on the surface promote not fully molten materials; hence creating a keyhole pore. To account for this, the higher exposure time should correspond accordingly to higher scanning speeds. The best combination has been found for a scan speed of 457.1 mms^{-1}, hatch spacing 80 µm, and 200 W laser power when using a layer thickness of 35 µm and employing the pre-sinter scan strategy yielding a mean density of 98.7%.

The main porosity conclusions summarise as follows:

- Densities of AlSi10Mg fabricated parts are relatively high (reached 99.24%). Moreover, the study has confirmed that density increases gradually with the increase of exposure time as it reduces the scan speed, and thus increases energy density accordingly as clarified in Equation 2.2. When the exposure time is 175, density is at its maximum. Otherwise, too short exposure times would lead to a density reduction.

- Energy density has an important influence on the part's surface morphology. Too high or too low ϕ values could leave defects and allow for a potential formation of micro-cracks.

Progress Review Presentation (view)

Bibliography

Abele, Eberhard and Kniepkamp, Michael (2015). "Analysis and optimisation of vertical surface roughness in micro selective laser melting". In: *Surface Topography: Metrology and Properties* 3.3, p. 034007.

Aboulkhair, Nesma T, Everitt, Nicola M, Ashcroft, Ian, and Tuck, Chris (2014). "Reducing porosity in AlSi10Mg parts processed by selective laser melting". In: *Additive manufacturing* 1, pp. 77–86.

Boschetto, Alberto, Bottini, Luana, and Veniali, Francesco (2017). "Roughness modeling of AlSi10Mg parts fabricated by selective laser melting". In: *Journal of Materials Processing Technology* 241, pp. 154–163.

Danzl, Reinhard, Helmli, Franz, and Scherer, Stefan (2011). "Focus variation–a robust technology for high resolution optical 3D surface metrology". In: *Strojniški vestnik-Journal of mechanical engineering* 57.3, pp. 245–256.

Greaves, George Neville, Greer, AL, Lakes, Roderic S, and Rouxel, Tanguy (2011). "Poisson's ratio and modern materials". In: *Nature materials* 10.11, pp. 823–837.

Hirata, Tomotake, Kimura, Takahiro, and Nakamoto, Takayuki (2020). "Effects of hot isostatic pressing and internal porosity on the performance of selective laser melted AlSi10Mg alloys". In: *Materials Science and Engineering: A* 772, p. 138713.

Kempen, K, Thijs, L, Yasa, E, Badrossamay, M, Verheecke, W, and Kruth, JP (2011). "Process optimization and microstructural analysis for selective laser melting of AlSi10Mg". In: *Solid Freeform Fabrication Symposium*. Vol. 22. 2011, pp. 484–495.

Larrosa, NO, Wang, W, Read, N, Loretto, MH, Evans, C, Carr, J, Tradowsky, U, Attallah, MM, and Withers, PJ (2018). "Linking microstructure and processing defects to mechanical properties of selectively laser melted AlSi10Mg alloy". In: *Theoretical and Applied Fracture Mechanics* 98, pp. 123–133.

Leary, M (2017). "Surface roughness optimisation for selective laser melting (SLM): accommodating relevant and irrelevant surfaces". In: *Laser additive manufacturing*. Elsevier, pp. 99–118.

Lees, Caroline, Vincent, Julian FV, and Hillerton, J Eric (1991). "Poisson's ratio in skin". In: *Bio-medical materials and engineering* 1.1, pp. 19–23.

Leon, Avi and Aghion, Eli (2017). "Effect of surface roughness on corrosion fatigue performance of AlSi10Mg alloy produced by Selective Laser Melting (SLM)". In: *Materials Characterization* 131, pp. 188–194.

Li, Bao-Qiang, Li, Zhonghua, Bai, Peikang, Liu, Bin, and Kuai, Zezhou (2018). "Research on surface roughness of AlSi10Mg parts fabricated by laser powder bed fusion". In: *Metals* 8.7, p. 524.

Manufacturers, Sensofar (2021). *Sensofar Optical Profilometer*. URL: `https://www.sensofar.com/` (visited on 2021).

Martin, John H, Yahata, Brennan D, Hundley, Jacob M, Mayer, Justin A, Schaedler, Tobias A, and Pollock, Tresa M (2017). "3D printing of high-strength aluminium alloys". In: *Nature* 549.7672, pp. 365–369.

Pastre, Marc-Antoine de, Thompson, Adam, Quinsat, Yann, Garcıa, José A Albajez, Senin, Nicola, and Leach, Richard (2020). "Polymer powder bed fusion surface texture measurement". In: *Measurement Science and Technology* 31.5, p. 055002.

Read, Noriko, Wang, Wei, Essa, Khamis, and Attallah, Moataz M (2015). "Selective laser melting of AlSi10Mg alloy: Process optimisation and mechanical properties development". In: *Materials & Design (1980-2015)* 65, pp. 417–424.

Senin, Nicola, Thompson, Adam, and Leach, Richard K (2017). "Characterisation of the topography of metal additive surface features with different measurement technologies". In: *Measurement Science and Technology* 28.9, p. 095003.

Strano, Giovanni, Hao, Liang, Everson, Richard M, and Evans, Kenneth E (2013). "Surface roughness analysis, modelling and prediction in selective laser melting". In: *Journal of Materials Processing Technology* 213.4, pp. 589–597.

Thompson, Adam, Senin, Nicola, Giusca, Claudiu, and Leach, Richard (2017). "Topography of selectively laser melted surfaces: a comparison of different measurement methods". In: *CIRP Annals* 66.1, pp. 543–546.

Tiwari, Jitendar Kumar, Mandal, Ajay, Sathish, N, Agrawal, AK, and Srivastava, AK (2020). "Investigation of porosity, microstructure and mechanical properties of additively manufactured graphene reinforced AlSi10Mg composite". In: *Additive Manufacturing* 33, p. 101095.

Wong, Kaufui V and Hernandez, Aldo (2012). "A review of additive manufacturing". In: *International scholarly research notices* 2012.

Yu, Wenhui, Sing, Swee Leong, Chua, Chee Kai, and Tian, Xuelei (2019). "Influence of re-melting on surface roughness and porosity of AlSi10Mg parts fabricated by selective laser melting". In: *Journal of Alloys and Compounds* 792, pp. 574–581.

Appendix A

Appendix - Nomenclature

Table A.1: Nomenclature

Symbol	Quantity	Unit
a_p	Contact Radius	m
E	Young's Modulus	Pa
E_T	Exposure Time	µs
F	Force	N
H_S	Hatch Spacing	µm
L	Length	m
P	Power	W
P_D	Point Distance	µm
P_p	Hardness	MPa
R	Radius	µm
R^2	Coefficient of Determination	–
S_a	Arithmetic Mean Height	µm
S_q	Root mean Square Height	µm
S_{sk}	Skewness	µm
S_{ku}	Kurtosis	µm
S_p	Maximum Peak Height	µm
S_v	Maximum Pit Height	µm
S_z	Maximum Height	µm

Table A.2: Nomenclature

Symbol	Quantity	SI Unit
t	Layer Thickness	µm
ν	Poisson's Ratio	–
v	Scan Speed	mms^{-1}
w	Applied Contact Load	N
w_c	Critical Load	N
w_o	Load at the onset of plastic yield	N
x	Position	m

Appendix B

Appendix - Raw Data

B.1 Experimental Apparatus

Table B.1: Roughness Testing Apparatus.

Aluminium Samples
27 Alumnimum AlSi10Mg 10 mm^3 cubes
Non-Contact Surface Device
Optical Profilometer (Sensofar SMART device)
Magnifying Lenses
10× and 50× Magnifying Objective Lenses
Cube Sample Holder
3D printed ABS plastic (for specimen positioning at the centre)
Stitching and Image Processing
MountainsMap and SensoMap Software
Data Processing
Mondrian, SPSS, R, and JAVA

Table B.2: Polishing and Porosity Apparatus.

Sectioned Aluminium Samples
81 Sectioned AlSi10Mg Rectangular Prisms
Mounting Press
Struers Lab Mounting Press Primopress
Mechanical Grinder
Struers STELLAPOL Polisher
Grinding Wheels
P240 and P400 Silicon Carbide Abrasive Paper (SiC) and a Micro Polishing Cloth
Polishing Liquids
6 and 3 µm Diamond Liquid Metal Polish and Colloidal Silica Polishing Gel
Microscope
Leica-DM500 Microscope attached to a 5× Lens
Image Processing
MATLAB, and ImageJ software

B.2 AM AlSi10Mg Manufacturing Data

Coded Values	Point Distance	Exposure Time	Hatch spacing	Exposures
sample	P_d	T_e	h	e
1	-1	-1	0	0
2	-1	1	0	0
3	1	-1	0	0
4	1	1	0	0
5	0	0	-1	-1
6	0	0	-1	1
7	0	0	1	-1
8	0	0	1	1
9	-1	0	0	-1
10	-1	0	0	1
11	1	0	0	-1
12	1	0	0	1
13	0	-1	-1	0
14	0	-1	1	0
15	0	1	-1	0
16	0	1	1	0
17	-1	0	-1	0
18	-1	0	1	0
19	1	0	-1	0
20	1	0	1	0
21	0	-1	0	-1
22	0	-1	0	1
23	0	1	0	-1
24	0	1	0	1
25	0	0	0	0
26	0	0	0	0
27	0	0	0	0

Power	Exposures	Point Distance	Exposure Time	Scan Speed	Hatch Spacing	Layer Thickness	Energy Density
P /W	e	P_d /µm	T_e /µs	mm/s	h /µm	t /µm	ψ /Jmm^{-3}
200	2	60	105	571.4	80	35	125.0
200	2	60	175	342.9	80	35	208.3
200	2	100	105	952.4	80	35	75.0
200	2	100	175	571.4	80	35	125.0
200	0	80	140	571.4	60	35	166.7
200	4	80	140	571.4	60	35	166.7
200	0	80	140	571.4	100	35	100.0
200	4	80	140	571.4	100	35	100.0
200	0	60	140	428.6	80	35	166.7
200	4	60	140	428.6	80	35	166.7
200	0	100	140	714.3	80	35	100.0
200	4	100	140	714.3	80	35	100.0
200	2	80	105	761.9	60	35	125.0
200	2	80	105	761.9	100	35	75.0
200	2	80	175	457.1	60	35	208.3
200	2	80	175	457.1	100	35	125.0
200	2	60	140	428.6	60	35	222.2
200	2	60	140	428.6	100	35	133.3
200	2	100	140	714.3	60	35	133.3
200	2	100	140	714.3	100	35	80.0
200	0	80	105	761.9	80	35	93.8
200	4	80	105	761.9	80	35	93.8
200	0	80	175	457.1	80	35	156.3
200	4	80	175	457.1	80	35	156.3
200	2	80	140	571.4	80	35	125.0
200	2	80	140	571.4	80	35	125.0
200	2	80	140	571.4	80	35	125.0

B.3 Areal Roughness and Porosity Measurements

	Longitudenal Mean Porosity	Transverse Mean Porosity	Sa	Sq	Ssk	Sku	Sp	Sv	Sz
Samples			µm	µm	<no unit>	<no unit>	µm	µm	µm
1	313.75	163.5	16.4326	24.0265	0.64425	7.69888	150.587	110.29	260.877
2	240	321.5	17.6268	28.3105	2.50316	13.9717	204.962	105.938	310.9
3	210.75	167	10.2441	14.854	1.42933	8.2189	105.645	62.4029	168.047
4	323.25	123.5	20.1809	30.2325	1.09703	6.69119	174.447	131.886	306.333
5	323.75	248	12.0368	23.4356	3.23604	18.7806	160.179	84.0132	244.192
6	160.5	258	11.0475	17.2142	2.47275	14.8325	147.657	73.637	221.294
7	268	187	19.8416	29.1022	1.63228	8.94075	169.829	155.038	324.867
8	249.75	375	15.4467	23.1875	1.62678	11.799	162.865	104.798	267.662
9	261.75	388	10.5514	15.9909	0.24777	7.88351	126.959	83.5912	210.55
10	97.75	111.5	11.5875	17.0034	1.09378	9.07537	120.811	105.716	226.527
11	223	189	9.62643	13.7127	0.8868	9.20699	120.016	82.4243	202.441
12	114.5	144	11.8305	18.8442	1.88461	11.4414	145.874	71.8831	217.757
13	249	76	18.371	32.515	2.94375	16.8249	233.612	105.485	339.097
14	156	159.5	14.8966	22.1785	0.92741	8.5644	161.669	179.948	341.617
15	137.75	123.5	13.6222	18.7628	0.30777	5.83755	108.779	108.448	217.227
16	320.25	308.5	21.3735	32.5309	1.47348	11.6607	242.013	125.26	367.273
17	267	169	8.73195	13.5157	2.34407	12.5909	125.644	64.3773	190.022
18	410.5	557	6.80879	10.5619	2.09852	14.3317	90.2894	60.17	150.459
19	117.75	116.5	12.9847	19.6193	1.49673	11.8401	138.157	93.745	231.902
20	287.75	104.5	9.49269	13.7111	1.59919	9.61057	138.373	49.2982	187.671
21	186	212	9.26426	14.1293	2.69076	21.6209	148.78	58.7317	207.512
22	139.5	192	19.4022	28.0651	0.94264	6.55196	166.838	115.393	282.231
23	171	89	20.5543	34.8274	3.13382	17.3431	245.272	122.534	367.806
24	123.75	126.5	10.5679	14.9483	1.17944	6.98262	101.567	67.8549	169.422
25	123.75	86	24.3428	44.5483	3.55288	17.2765	304.666	69.6813	374.347
26	138	230.5	6.44575	9.31234	1.56863	13.3264	102.743	54.2741	157.017
27	330	249.5	9.87572	14.2869	1.08644	10.2493	133.968	57.864	191.832

B.4 Roughness and Porosity Processed Data

B.4.1 Roughness

Table B.3: S_q Analysis of variance (ANOVA) Three-way result.

Source	DoF	Sum of Squares	Mean Squares	F-calculated	Significance	PCR
P_D	2	118.47	59.24	0.74	0.61	7.45
H_S	2	60.20	30.10	0.37	0.74	3.79
E_T	2	111.91	55.95	0.70	0.51	7.04
$P_D \times H_S$	4	54.30	13.58	0.17	0.70	3.42
$P_D \times E_T$	4	420.18	105.04	1.31	0.53	26.44
$E_T \times H_S$	4	181.50	45.38	0.56	0.95	11.42
Error	8	642.85	80.36			40.45
Total	26	1,589.41				100

Table B.4: Sz Analysis of variance (ANOVA) Three-way result.

Source	DoF	Sum of Squares	Mean Squares	F-calculated	Significance	PCR
P_D	2	2,753.52	1,376.76	0.22	0.8088	2.84
H_S	2	4,803.77	2,401.88	0.38	0.6955	4.96
E_T	2	876.69	438.35	0.07	0.9335	0.91
$P_D \times H_S$	4	12,090.08	3,022.52	0.48	0.7515	12.49
$P_D \times E_T$	4	15,705.64	3,926.41	0.62	0.6601	16.22
$E_T \times H_S$	4	10,041.44	2,510.36	0.40	0.8056	10.37
Error	8	50,552.47	6,319.06			52.21
Total	26	96,823.62				100

B.4.2 Porosity

Table B.5: Lowest Transverse Porosity values.

	Transverse Porosity	Manufacturing Parameters	v/mm^{-1}	ϕ/Jmm^{-3}
S13	0.76%	$P_D = 80$, $E_T = 105$, and $H_S = 60$	761.9	125
S25	0.86%	$P_D = 80$, $E_T = 140$, and $H_S = 80$	571.4	125
S23	0.89%	$P_D = 80$, $E_T = 175$, and $H_S = 80$	457.1	156.3
S20	1.04%	$P_D = 100$, $E_T = 140$, and $H_S = 100$	457.1	156.3
S10	1.12%	$P_D = 60$, $E_T = 140$, and $H_S = 80$	457.1	156.3

* Values ranged within (2 – 7.2%) in respect to transverse lowest porosity.

Table B.6: Lowest Longitudinal Porosity values.

	Longitudinal Porosity	Manufacturing Parameters	v/mm^{-1}	ϕ/Jmm^{-3}
S10	0.98%	$P_D = 60$, $E_T = 140$, and $H_S = 80$	428.6	166.7
S12	1.15%	$P_D = 100$, $E_T = 140$, and $H_S = 180$	714.3	100.0
S19	1.18%	$P_D = 100$, $E_T = 140$, and $H_S = 60$	714.3	133.3
S24	1.24%	$P_D = 175$, $E_T = 105$, and $H_S = 80$	457.1	156.3
S25	1.24%	$P_D = 140$, $E_T = 105$, and $H_S = 80$	571.4	125.0

* Values ranged within (5.4 – 8.3%) in respect to transverse lowest porosity.

Table B.7: Longitudinal Direction (ANOVA) Three-way result.

Source	DoF	Sum of Squares	Mean Squares	F-calculated	Significance	PCR
P_D	2	0.48	0.24	0.35	0.7135	2.89
H_S	2	1.84	0.92	1.34	0.3151	10.97
E_T	2	1.57	0.79	1.14	0.3661	9.36
$P_D \times H_S$	4	3.76	0.94	1.37	0.3269	22.38
$P_D \times E_T$	4	1.14	0.29	0.41	0.7938	6.80
$E_T \times H_S$	4	2.50	0.62	0.91	0.5040	14.85
Error	8	5.51	0.69			32.76
Total	26	16.81				100

B.5 Hatch Spacing Calculation

In reference to Equation 2.2, rearranging for H_S:

$$H_S = \frac{\mathrm{P}}{v \times \phi \times t}$$

Substituting in values for P, v, ϕ, and t:

$$H_S = \frac{200}{457.1 \times 156.25 \times 35 \times 10^{-6}}$$

$$H_S = 80\mu\mathrm{m}$$